

On Computational Entanglement and Its Interpretation in Adversarial Machine Learning

YenLung Lai, XingBo Dong, and Zhe Jin

Abstract—Adversarial examples in machine learning has emerged as a focal point of research due to their remarkable ability to deceive models with seemingly inconspicuous input perturbations, potentially resulting in severe consequences. In this study, we embark on a comprehensive exploration of adversarial machine learning models, shedding light on their intrinsic complexity and interpretability. Our investigation reveals intriguing links between machine learning model complexity and Einstein’s theory of special relativity, through the concept of entanglement. More specific, we define entanglement computationally and demonstrate that distant feature samples can exhibit strong correlations, akin to entanglement in quantum realm. This revelation challenges conventional perspectives in describing the phenomenon of adversarial transferability observed in contemporary machine learning models. By drawing parallels with the relativistic effects of time dilation and length contraction during computation, we gain deeper insights into adversarial machine learning, paving the way for more robust and interpretable models in this rapidly evolving field.

Index Terms—Adversarial Machine Learning, Entanglement, Complexity, Information Reconciliation



1 INTRODUCTION

The rise of machine learning has increased reliance on automated systems for critical decision-making across various domains, particularly in pattern recognition, enabling the identification and classification of objects and individuals through biometric recognition. However, this integration of machine learning in pattern recognition brings advantages and significant concerns.

Started from 2004, Dalvi et al. [1] and quickly followed by Lowd and Meek [2] exposed the susceptibility of linear classifiers to adversarial manipulations in spam filtering, marking the early instances of adversarial attacks. In 2006, Barreno et al. [3] presented a taxonomy of attacks on machine learning systems, while Biggio et al. [4] demonstrated gradient-based attacks. In 2012, Szegedy et al. [5] revealed the vulnerability of deep neural networks to gradient-based attacks, introducing *adversarial examples* that closely resemble original data but can lead to incorrect model predictions. These findings highlight the risks inherent in machine learning systems, especially in pattern recognition tasks. Adversarial attacks can exploit model vulnerabilities, casting doubt on their trustworthiness and suitability for critical decision-making processes.

Adversarial Example: Adversarial examples introduce a noteworthy attribute, which is the ability to deceive disparate machine learning models despite differences in their architectures or training datasets. Furthermore, when these different models are deceived by an adversarial example, they tend to agree with each other on the incorrect class prediction. This transferability phenomenon challenges the conventional belief that models with varying characteristics would possess diverse vulnerabilities and make dissimilar

errors [6]. It also implies the existence of common vulnerabilities or analogous decision boundaries across diverse models. Despite their differences, these models may possess susceptibility to similar input perturbations or exhibit similar decision-making mechanisms that are sensitive to adversarial manipulations. The transferability of adversarial examples raises concerns about the robustness and generalizability of machine learning models, whereby an attacker is able to train their own substitute model, generate adversarial examples against the substitute, and successfully exploit the vulnerabilities of a victim model with minimal knowledge about it.

Research by Papernot et al. [7] provides substantial evidence supporting the transferability of adversarial examples, even in black-box scenarios. Within these environments, an adversary does not possess detailed knowledge about the internal intricacies of the model, such as its architecture or specific parameter values. Interactions with the model are solely confined to supplying input data and observing the corresponding predicted labels. This paradigm sets forth a realistic, yet formidable, challenge, as adversaries often lack a comprehensive understanding of the model’s intricate operations. Their study substantiates the potential of black-box attacks, showcasing their practical feasibility across an extensive range of machine learning models. The models considered in their study have span beyond deep neural networks (DNNs) and encompass logistic regression (LR), support vector machines (SVM), decision trees (DT), and k-nearest neighbors (kNN).

Indeed, extensive research has been conducted to investigate the transferability phenomenon, and numerous theories have emerged to explain its underlying mechanics. These theories commonly posit that adversarial examples occur due to complex and high dimensional inconsistencies present in the training data [8]–[10]. Nevertheless, these theories have yet to provide a complete understanding that succinctly portrays how this phenomenon operates in

YenLung Lai, XingBo Dong, and Zhe Jin are with Anhui Provincial Key Laboratory of Secure Artificial Intelligence; Anhui Provincial International Joint Research Center for Advanced Technology in Medical Imaging, School of AI, Anhui University, Hefei 230093, China. (e-mail: {yenlung, xingbo.dong, jinzhe}.ahu.edu.cn)

practical settings.

Despite the incomplete understanding of adversarial transferability’s root cause, the drive to maximize machine learning model accuracy has shown no signs of slowing down [11], [12]. This belief in accuracy improvement as a means to enhance adversarial robustness is unyielding. However, it’s important to note that while accuracy improvement is a significant goal, it doesn’t guarantee adversarial robustness. Ilyas et al. [13] emphasized this in their work, suggesting that human-understandable explanations closely tied to model training are essential. They introduced a fresh perspective, arguing that adversarial examples stem from a model’s sensitivity to data features with strong generalization properties, not anomalies. They position adversarial vulnerability as a human-centric issue, asserting that in standard supervised learning, both non-robust and robust features play equally vital roles in shaping model predictions.

Recent research conducted by Ambra Demontis et al. [14] has revealed the relationship between the transferability of adversarial examples and the complexity of models. The study indicates that higher complexity models are more susceptible to the transfer of adversarial examples. This susceptibility can be attributed to the greater gradients observed in more complex models, which represent the rate of change of the loss function. Loosely speaking, as the complexity of a model increases, the potential for adversarial examples to successfully transfer and deceive the model also tends to increase with appropriate regularization applied.

While these findings may seem counter-intuitive, it’s important to consider the trade-offs. As models increase in complexity, they can become less transparent and harder to intuitively understand. This is especially true for deep learning models with highly non-linear neural network architectures. This interpretability challenge makes it even harder for researchers to fully grasp the transferability of adversarial examples. Therefore, in the rapidly developing field of adversarial machine learning, there’s a real need for practical research and solutions that address this issue.

Summary of Results: In this study, we focus on adversarial machine learning models, emphasizing interpretability, complexity, and their impact on model accuracy. Our research is motivated by the lack of powerful adversarial models for reference. We highlight the importance of a strong adversarial model that can overcome computational limitations to understand adversaries’ objectives in attacking machine learning models.

Our research deviates from traditional error correction approaches and is deeply rooted in physical laws, particularly the second law of thermodynamics, which posits an ever-increasing system entropy. To counteract this entropy surge, we introduce the concept of computational entanglement in machine learning: for deterministic computation of model parameters (ensuring model correctness) and for preserving system information through encoding (guaranteeing model completeness). Deeper analysis reveals connections between our model and Einstein’s theory of special relativity. In particular, our demonstration showcases that through entanglement is sufficient to establish a flat spacetime framework for the study of relative motion between objects. Our findings propose that increasing complexity

serves as the fundamental principle to ensure the consistency of physical laws across all inertial frames of reference. Intriguingly, this new discovery resonates with the work by Brown and Susskind in 2018 [15]. While they proposed a growth in quantum complexity as a fundamental physical law, our observed increase in complexity is rooted purely in classical terms.

Beyond theoretical implications, the computational manifestation of entanglement enables us to simulate entanglement using real-valued sample features. We demonstrate that entanglement can manifest in any arbitrary random distribution, resulting in effects like time dilation and length contraction as information encoding continues with increasing computational complexity. As the complexity increases, such relativistic phenomena inadvertently shrinks the distinctions between distinct features, paving the way for adversarial examples that could result in potential misclassification.

Based on our findings, we hope to ignite fresh enthusiasm and contribute to evolving perspectives on entanglement in both the machine learning and physics communities. This exploration holds the promise of enhancing the robustness of machine learning models and providing valuable insights into enduring mysteries, such as spacetime expansion and the manifestation of quantum entanglement in spacetime.

2 CONTEMPORARY CHALLENGES IN TODAY’S MACHINE LEARNING MODELS

In machine learning, it’s often thought that the more complex the model, the better its accuracy. This belief has led to a push for advanced, ‘black box’ learning models to get the best prediction performance possible [16]. The research of Zhang et al. [17] further illuminates this concept by demonstrating that neural networks are capable of learning arbitrary relationships between images and labels. This remains true even when these models are subjected to stringent regularization techniques, and when original images are replaced with random, unstructured noise, contradicting conventional expectations. Furthermore, they establish through theoretical construction that even simple, two-layer neural networks can perfectly fit the data once the number of parameters surpasses the number of data points. Therefore, it appears that model complexity is proportional to accuracy, given the direct correlation between the increase in the number of parameters and enhanced learning performance. This gives rise to an intriguing question: *Should machines delve into acquiring features that may not align with human perceptions of usefulness in pursuit of peak accuracy?*

In order to tackle this query, we first need to establish what signifies a “useful” feature from a human perspective within the realm of machine learning. This definition largely hinges on the specific context and the problem at hand. Broadly speaking, a feature is regarded as useful if it substantially improves the model’s predictive capability and aligns with human interpretability [18]. Human interpretability typically involves features that align with our understanding of the problem domain. For example, in a predictive model for housing prices, variables like square footage, geographic location, and the number of bedrooms

are considered meaningful and interpretable to humans due to our awareness of their impact on property values.

However, machine learning models, particularly deep learning ones, are known to identify non-robust features—those which humans find challenging to comprehend or regard as insignificant. While these features often contribute to high model generalization, they render the models susceptible to adversarial attacks. The study conducted by Ilyas et al. [13] suggests a nuanced understanding of non-robust features in models, arguing that they are not inherently “useless”. Rather, their functionality resides in regions that might not align with human intuition or contemplation. Such features are essential when the ultimate goal is achieving the highest possible accuracy.

Rudin [19] asserts that while uninterpretable algorithms can still prove beneficial in high-stakes decisions as part of the knowledge discovery process (for instance, to establish baseline performance levels), they are generally not the final objective of knowledge discovery. The need for model interpretability becomes particularly crucial in high-stakes applications such as medicine, judicial decision-making, autonomous driving, among others—it is imperative not only for a model to be accurate but also to be interpretable. An interpretable model affords users an understanding of why it is rendering certain predictions, fostering trust in the model, and facilitating scrutiny and justification of its decisions.

Research has indicated that the differences in performance among various algorithms tend to be negligible if a standard knowledge discovery process is followed. This implies that high accuracy in machine learning models can be achieved without necessarily sacrificing interpretability, provided that appropriate data preparation steps, including feature engineering, are conducted effectively [20], [21].

While accuracy and interpretability are important, another crucial aspect of machine learning models is their robustness against adversarial attacks. In this context, the perspective of an adversary is essentially about understanding the potential vulnerabilities and weak points of a model. By adopting this perspective, data scientists can design machine learning models that are less susceptible to such attacks and are more robust in general. Yet, there seems to be a deficit in the field concerning comprehensive adversary models that can illustrate all possible threats an adversary might pose to a machine learning model. Such models are critical as they give a holistic perspective on what an attacker might ultimately aim for, regardless of the type of attack model, be it under a black-box or a white-box setting. Therefore, a comprehensive understanding of potential adversarial threats is vital. Achieving a balance between model accuracy, complexity, and interpretability ensures our models are not only precise but also interpretable for continuous improvement. This balance shall fortifies the models’ resilience against adversarial intrusions, thereby enhancing their overall effectiveness and security.

3 DEFINITION: INFORMATION THEORETIC ADVERSARIAL LEARNING MODEL

We begin with the definition of an information theoretic adversarial learning model, which is characterized by pa-

rameter inference, a vital yet longstanding concept in machine learning, without making additional assumption over the computational power of the adversary. More specific, it follows the Bayesian inference (a.k.a Bayes’s Theorem) that combines prior beliefs of arbitrary random distribution \mathcal{D} with observed data $x \in \mathcal{D}$, to offer precise uncertainty measures for achieving model objective.

Adversary Model’s Objective: By means of parameter inference, the objective of the defined model is to identify a parameter value, denoted as θ_0 , that maximize the posterior probability $P(\theta_0 = \theta | \mathcal{D})$, given an arbitrary random distribution, denoted as \mathcal{D} . As parameters are fundamentally essential in characterizing *almost all* machine learning model. A precise inference of the true parameter provides an adversary with the tools necessary to launch an attack across various models. We here consider the true parameter, denoted as θ_0 , to be unknown; if it were otherwise, there would be no problem to resolve. The primary objective is to maximize the likelihood of an inferred parameter, θ , being identical to the true parameter θ_0 . Using Bayes’ Theorem, it can be formally described as:

$$P(\theta = \theta_0 | \mathcal{D}) = \frac{P(\mathcal{D} | \theta = \theta_0) \cdot P(\theta = \theta_0)}{P(\mathcal{D})} \quad (1)$$

In above equation, $P(\mathcal{D} | \theta = \theta_0)$ represents the “likelihood” of the distribution \mathcal{D} given the inferred parameter θ . The term $P(\theta = \theta_0)$, known as the “prior”, reflects our initial belief concerning the value of θ prior to any data observation. The denominator $P(\mathcal{D})$, or the “evidence”, serves as a normalizing constant which ensures the probabilistic coherence of the equation. Disregarding the denominator could lead to the right-hand side of the equation failing to constitute a probability, thereby not necessarily falling between 0 and 1.

In the following paragraph, we demonstrate that the adversary model’s objective can be achieved through maximizing the likelihood, which ultimately represents the binary entropy of the true parameter θ_0 .

Likelihood Maximization: Given any training sample $x \in \mathcal{D}$, we can identify an explicit function f within \mathcal{F} , which maps the sample statistic to θ , that is $\theta = f(x_1, \dots, x_N)$ holds true for all x within \mathcal{D} . However, if this is not achievable, we should resort to numerical optimization. In this case, we choose the parameter value of θ that maximizes the likelihood of the data in order to fulfil our objective. In a conventional machine learning model, the process of maximization can be represented as follows:

$$\hat{\theta} = \arg \max_{\theta} \mathcal{L}(\theta; \mathcal{D}),$$

where $\hat{\theta}$ is our inferred parameter, and the likelihood typically referred to as joint density of $x \in \mathcal{D}$ that described as a function of θ expressed as:

$$\begin{aligned} \mathcal{L}(\theta; \mathcal{D} = x_1, \dots, \mathcal{D} = x_N) \\ &= f(\mathcal{D} = x_1, \dots, \mathcal{D} = x_N; \theta_1, \dots, \theta_N) \\ &= \prod_{i=1}^N f(\mathcal{D} = x_i; \theta_i) = \prod_{i=1}^N f(\mathcal{D} = x_i; \theta). \end{aligned} \quad (2)$$

The last line follows a common assumption used in machine learning that all training samples $(x_1, \dots, x_N) \in \mathcal{D}$ are independent and identically distributed (i.i.d).

Notably, the maximization of the likelihood can be done by minimizing the “negative log likelihood”, that is:

$$-\frac{1}{N} \log \mathcal{L}(\theta; \mathcal{D}) = -\frac{1}{N} \sum_{i=1}^N \log(f(\mathcal{D} = x_i; \theta)), \quad (3)$$

where we take the average via dividing the likelihood by $1/N$.

It should be noted that directly solving the minimization problem as stated above would not provide a meaningful result because it does not give us any information about the true distribution of \mathcal{D} . The true distribution should correspond to the true parameter θ_0 . Therefore, we employ a mathematical strategy of adding zero to the above equation, i.e., adding and subtracting the log-likelihood of $\log(f(\mathcal{D} = x_i; \theta_0))$. Consequently, bringing the negative term inside, we yield the following expression:

$$\frac{1}{N} \left[\sum_{i=1}^N \log \left(\frac{f(\mathcal{D} = x_i; \theta_0)}{f(\mathcal{D} = x_i; \theta)} \right) - \sum_{i=1}^N \log(f(\mathcal{D} = x_i; \theta_0)) \right] \quad (4)$$

For all $x \in \mathcal{D}$, with sufficiently large N , Eq. 4 converges to its expected value according to the asymptotic equipartition theorem, result to:

$$D_{KL}(f(x; \theta_0) || f(x; \theta)) + H(f(x; \theta_0)) \quad (5)$$

where

$$\begin{aligned} H(f(x; \theta_0)) &= -\mathbb{E}[\log(f(x; \theta_0))] \\ &= -\int_{\mathbb{R}} f(x; \theta_0) \log(f(x; \theta_0)) dx \end{aligned}$$

is the differential entropy of the true distribution $f(x; \theta_0)$ and

$$D_{KL}(f(x; \theta_0) || f(x; \theta)) = \int_{\mathbb{R}} f(x; \theta_0) \log \left(\frac{f(x; \theta_0)}{f(x; \theta)} \right) dx$$

is the Kullback-Leibler (KL) divergence, i.e., relative entropy between the true density ($f(x; \theta_0)$) and the parameter-inferred density ($f(x; \theta)$), which is a positive term and equal to zero only if $\theta = \theta_0$.

The optimal goal for the adversary is to attain $\theta = \theta_0$, where this leads us to the average minimum negative log likelihood equivalent to

$$-\frac{1}{N} \log \mathcal{L}(\theta; \mathcal{D}) = H(f(x; \theta_0)). \quad (6)$$

Non-Deterministic Limitations of Standard Approaches:

Noting that our defined adversary model is information theoretic, applicable to any machine learning model aiming to minimize the loss function or maximize likelihood. Yet, achieving $\theta = \theta_0$ in practice can be challenging due to factors like model complexity and noise, resulting in non-zero Kullback-Leibler divergence. Most importantly, the entropy of the likelihood function described above is non-deterministic, and cannot be further reduced without precise knowledge of the density function $f(\cdot)$ itself, that is, by setting its derivative to zero. For this outlined reason, we discern a theoretical constraint imposed by conventional optimization strategies in minimizing the negative log likelihood function. This limitation drives us to explore an alternative approach: employing coding approach [22] that involves transforming feature samples into

higher-dimensional codewords with the aim of ensuring the model’s correctness and completeness in the inference of arbitrary parameters $\theta_1, \theta_2, \dots$ discussed in the following sections.

4 MODEL’S CORRECTNESS AND COMPLETENESS

We begin by formalizing the model’s “correctness,” which refers to our confidence in predicting outcomes or generating adversarial examples. It provides insight into the likelihood of accurately inferring a parameter, ensuring that $\theta = \theta_0$ holds across various random inputs. This concept also encompasses the possibility of “transferability” characteristic of adversarial examples, where an effective attack against one model is likely to work against others.

4.1 Model’s Correctness

To formalize correctness within our adversarial models, we must explore non-robust features, as defined by Ilyas et al. [13], which are believed to serve as the primary reason for the transferability of adversarial examples across different learning models.

In our context, we redefine non-robust features as those with low real-world occurrence probabilities. This definition is intuitive because rare or infrequent features can be challenging for humans to recognize across various domains. However, it’s crucial to note that a feature’s robustness isn’t solely based on its occurrence probability. Instead, it relates more to how significantly the feature influences the model’s predictive performance. An infrequent feature may have a substantial impact on predictions when present, making it robust in terms of model accuracy. Conversely, a common feature may have little influence on outcomes, rendering it non-robust despite its high occurrence probability. Nevertheless, our reformulation emphasizes that a feature’s robustness depends on the model’s capability to detect its presence and understand its impact. This consideration, particularly relevant for adversarial examples, is vital for improving a model’s ability to effectively learn from and predict such features.

To account for these low probability (non-robust) features in our adversarial model, we focus on the distribution of distances between features. However, when adopting a coding approach, we typically view a feature sample, analogous to a message, as its corresponding codeword after the encoding process. Typically, the feature sample exists in a lower dimension k compared to its codeword dimension n , that is $k < n$. A smaller distance between codewords suggests a stronger correlation (i.e., intraclass) between their original features, while a larger distance implies a weaker correlation (i.e., interclass) their original features. To align with the discrete notion of conventional coding approaches [22], we denote $x = d_H(c, c'), \forall c \in \mathcal{C} \in \{-1, 1\}^n$ as the Hamming distance between the codewords post quantization. The term ‘quantization’ refers to quantizing the codeword values by their sign into the set $\{-1, 1\}$, creating n -dimensional binary vectors in \mathcal{C} where

$$\Pr[x = k] = \theta^k (1 - \theta)^{n-k}. \quad (7)$$

4.1.1 Interpreting Models in the Context of Second Law of Thermodynamics and Entanglement

The annotation in Eq. 7 narrows our attention to those distributions that can be described with the inferred parameter θ , with codewords distance equal to k . This annotation is crucial as it describes arbitrary codewords distance $x \in \mathcal{D}$ as an i.i.d Binomial variable characterized by θ . While that is common for standard machine learning models to assume that training data is i.i.d without additional constrain; However, this assumption can be quite idealistic which often doesn't hold in practical applications. Users might introduce manipulated data that violates this i.i.d assumption [23] potentially allow transferability of adversarial examples across different models [24].

In the context of the aforementioned, we can describe the density $f(x; \theta)$ corresponds to the inferred parameter (θ) as a function of (x, k, θ) follows:

$$f(x; \theta) \Rightarrow f(x, k; \theta) = \Pr[x = k] = \theta^k (1 - \theta)^{n-k}.$$

Given above description, it becomes logical to define the true density, which corresponds to θ_0 , as conforming to a Binomial distribution:

$$f(x; \theta_0) \Rightarrow f(x, k; \theta_0) = \binom{n}{k} \theta_0^k (1 - \theta_0)^{n-k}.$$

The reason for this formulation is to establish a rigorous relationship between the measured density and the true density function. This relationship can be written as follows:

$$\frac{f(x, k; \theta_0)}{f(x, k; \theta)} = \binom{n}{k} \quad (8)$$

if and only if $\theta = \theta_0$.

It's important to note that the equation above describes the relationship between a single true parameter, θ_0 , and a single inferred parameter, θ . However, for the sake of model completeness (will be elaborated in Section 4.2), we consider the possibility of using a finite number of parameters to describe the true densities of the system, i.e., $\theta_1, \theta_2, \dots, \theta_t$. This approach resembles the chain rule in calculus used to compute derivatives of composite functions. In our context, the end result is not a derivative but a derivable constant with respect to t . This constant arises from a sequence of fractions representing the true densities of the system, linked together similar to function compositions in the chain rule expressed as:

$$\begin{aligned} & \frac{f_0(x, k; \theta_0)}{f_0(x, k; \theta_1)} \frac{f_1(x, k; \theta_1)}{f_1(x, k; \theta_2)} \cdots \frac{f_{t-1}(x, k; \theta_{t-1})}{f_{t-1}(x, k; \theta_t)} \frac{f_t(x, k; \theta_t)}{f_t(x, k; \theta_t)} \\ &= \left(\frac{\binom{n}{k} \theta_0^k (1 - \theta_0)^{n-k}}{\binom{n}{k} \theta_1^k (1 - \theta_1)^{n-k}} \right) \left(\frac{\binom{n}{k} \theta_1^k (1 - \theta_1)^{n-k}}{\binom{n}{k} \theta_2^k (1 - \theta_2)^{n-k}} \right) \cdots \\ & \cdots \left(\frac{\binom{n}{k} \theta_{t-1}^k (1 - \theta_{t-1})^{n-k}}{\binom{n}{k} \theta_t^k (1 - \theta_t)^{n-k}} \right) \left(\frac{\binom{n}{k} \theta_t^k (1 - \theta_t)^{n-k}}{\binom{n}{k} \theta_t^k (1 - \theta_t)^{n-k}} \right) \\ &= \prod_{i=1}^t \frac{f_i(x, k; \theta_{i-1})}{f_i(x, k; \theta_i)} = \binom{n}{k} \left(\frac{\theta_0^k (1 - \theta_0)^{n-k}}{\theta_t^k (1 - \theta_t)^{n-k}} \right), \quad (9) \end{aligned}$$

if and only if $\theta_0 = \theta_1 = \dots = \theta_t$.

Our formalization significantly diverges from conventional machine learning models. In our approach, the inferred parameter with density $f(x, k; \theta)$ is a unique instance

of the true density, following a Binomial distribution, and is allowed to evolve, transitioning from a single case to $\binom{n}{k}$ possible cases. This ongoing process leads to an exponentially increasing constant, which we refer to as the "entanglement complexity". This constant encompasses all t parameters ($\theta_1, \dots, \theta_t$) that characterize the evolving system's true densities over time. We conveniently designate t as the "maximum encoding time step." An increase in t correlates with longer computation time, indicative of heightened computational complexity.

To gain more insight into the described entanglement effect, we explore the rationale behind formalizing densities corresponding to the same parameter. This transition, from $f_0(x, k, \theta_1)$ to $f_1(x, k, \theta_1)$, aligns with the principles of the *second law of thermodynamics*, indicating a tendency toward increased entropy within isolated systems until equilibrium is reached. However, our bold proposition challenges the notion that in equilibrium, the system's evolution ceases, drawing inspiration from the work of [15]. We formalize the system's ongoing evolution, considering its susceptibility to disturbances such as entanglement.

In this study, we computationally liken entanglement to an encoding process capturing the system's dynamically evolving states, such as the density transition from $f_1(x, k, \theta_1)$ to $f_1(x, k, \theta_2)$. These operations uphold the *principle of conservation of probability*, ensuring no critical information or relationships are lost, thus preserving order and completeness. This preservation allows the system to represent original states and their progression, resulting in entropy reduction. Following encoding, another density transition occurs, from $f_2(x, k, \theta_2)$ to $f_3(x, k, \theta_2)$, guided by the same underlying law, resulting in entropy increase.

Remarkably, this process can continue indefinitely and recursively, each step considering new entanglement with parameter θ_i based on preceding density state, leading to fluctuations in system entropy. Despite these densities are chained, the individual elements can be independently and identically analysed by slicing through each constant fraction, denoted as $f_i(\cdot)/f_i(\cdot)$ over individual encoding time step $i \in \{1, \dots, t\}$. In simpler terms, if one is able to determine θ_0 , they would also be able to ascertain the remaining $\theta_1, \dots, \theta_t$ due to their identical and independent characteristics. By following this line of reasoning, we conveniently omit the subscript for our annotation of θ and **shift our focus to the simplest case where we have only a single true parameter θ to consider**, as described in Eq. 8. Next, by substituting Eq. 8 into Eq. 4, we obtain the following result:

$$\begin{aligned} & \frac{1}{N} \sum_{i=1}^N \left[\log \binom{n}{k} - \log \left(\binom{n}{k} \theta_0^k (1 - \theta_0)^{n-k} \right) \right] \\ &= -\log((\theta_0)^k (1 - \theta_0)^{n-k}). \end{aligned}$$

The result derived above substantiates the proposition that the minimization problem, previously delineated in Eq. 3, can indeed be effectively reduced to the minimization of the negative log-likelihood of a specific Binomial distribution. In this context, the solution for θ_0 that maximize the likelihood can be determined by differentiating the negative logarithm of the aforementioned likelihood function with

respect to θ_0 and setting the resultant value to zero. This approach leads us to the following:

$$\begin{aligned} \frac{d(-\log((\theta_0)^k(1-\theta_0)^{n-k}))}{d\theta_0} &= 0 \\ \Rightarrow \left(\frac{\theta_0}{1-\theta_0} - \frac{k}{n-k} \right) &= 0 \\ \Rightarrow \theta_0 &= \frac{k}{n}, \end{aligned}$$

with $\theta_0 = k/n$ maximizes the likelihood function. This gives us the deterministic solution of average minimum negative log likelihood described as:

$$-\frac{1}{N} \log \mathcal{L}(\theta; \mathcal{D}) = nH_2(\theta_0) = nH_2(k/n) \quad (10)$$

where $H_2(\cdot)$ denotes the binary entropy function.

4.1.2 Explicit Model Construction: Encoding and Decoding

To explicitly construct the aforementioned model, we leverage the concept of Locality Sensitive Hashing (LSH) for encoding, to generate codewords that follow a Binomial distribution from arbitrary pairs of random feature samples.

Encoding via Cosine Distance-based LSH [25]: Given two random feature samples $w \in \mathbb{R}^k$ and $w' \in \mathbb{R}^k$, which can be normalized to vectors have unit norm. The Cosine Distance-based LSH defines individual functions $h_i(\cdot)$ using a randomly chosen normal unit vector $v_i \in \mathbb{R}^k$ and the Signum function $\text{sgn}(\cdot)$ for quantization. This is expressed as

$$h_i(w) = \text{sgn}(v_i^T \cdot w) \in \{-1, 1\}.$$

To ensure the independence of the functions $h_i(\cdot)$, it is crucial to draw their projection vectors v_i independently from the standard normal distribution with a mean of zero and a variance of one. Each $h_i(\cdot)$ produces a probability of difference between (w, w') in the hashed domain, which can be described as

$$\theta_0 = \frac{\sum_i^n h_i(w) \neq h_i(w')}{n} = \frac{\arccos(w \cdot w')}{\pi} \in (0, 1).$$

Let's formally define a generator function G . This function comprises a set of hash functions h_i , where $i \in \{1, \dots, n\}$. When we apply cosine distance-based LSH, the resulting output vector is referred to as an n -dimensional codeword. This codeword incorporates all $h_i \in G$:

$$\begin{aligned} c &= G(w) = (h_1(w), \dots, h_n(w)) \in \mathcal{C}, \\ c' &= G(w') = (h_1(w'), \dots, h_n(w')) \in \mathcal{C}, \end{aligned}$$

The Hamming distance, $x = d_H(c, c')$, between two codewords c and c' is found to conform to a Binomial distribution, denoted as $\text{Bin}(n, \theta_0)$. This relationship can be formulated as:

$$\Pr[x = k] = \binom{n}{k} (\theta_0)^k (1 - \theta_0)^{n-k}. \quad (11)$$

Owing to the Central Limit Theorem (CLT), when n is large, the Hamming distance $x = d_H(c, c')$ can be normalized, taking the form $(d_H(c, c') - n\theta_0) / \sqrt{n\theta_0(1 - \theta_0)}$, which tends to converge towards a standard normal distribution, $\mathcal{N}(0, 1)$. This observation implies that $d_H(c, c')$ aligns closely with a normal distribution, precisely $\mathcal{N}(n\theta_0, n\theta_0(1 - \theta_0))$ when

large enough n is in used. Given the *principle of maximum entropy*, the standard normal distribution, therefore, naturally serves as an optimal candidate for maximizing the entropy of the densities within our examination, supporting the model's interpretability in harmony with the second law of thermodynamics, as outlined in Eq. 9.

While adopting a normal distribution, which is inherently continuous, we introduce a derived set of measurements, termed "reduced codewords" denoted as follows:

$$\begin{aligned} \hat{c} &= \hat{G}(w) = (\hat{h}_1(w), \dots, \hat{h}_k(w)), \hat{c} \in \mathcal{C}^+ \\ \hat{c}' &= \hat{G}(w') = (\hat{h}_1(w'), \dots, \hat{h}_k(w')), \hat{c}' \in \mathcal{C}^+ \end{aligned}$$

Although it is not mandatory, it is beneficial to define each reduced codeword to be non-discrete ($\hat{c} \in \mathbb{R}^k$ and $\hat{c}' \in \mathbb{R}^k$) within a reduced dimensionality $k < n$ that aligns to their original sample (w, w') in \mathbb{R}^k . These reduced codewords are derived from a subset, namely "reduced matrix", $\hat{G} \subseteq G$ consisting of k hash functions drawn from the initial set G without any quantization. More specifically,

$$\hat{h}_i(w) = (v_i^T \cdot w) \in \mathbb{R}$$

for $i = 1, \dots, k$. This subset resides within a combinatorial codeword set— \mathcal{C}^+ —situated in the dimensionally reduced \mathbb{R}^k space.

To satisfy the necessary constraint established in Eq. 8, $f(x, k; \theta)$ should be expressed as a fraction, specifically $1/\binom{n}{k}$, of the true density $f(x, k; \theta_0)$. This implies that $f(x, k; \theta)$ represents a specified case, preferably the worst-case scenario of interest, among the $\binom{n}{k}$ possible outcomes of the true density. This aligns with our objective of configuring our model to effectively identify features with a low probability of occurrence that are located furthest from the origin of the standard normal distribution. In this context, our primary objective is to maximize the "relative distance" between the reduced codeword \hat{c} and \hat{c}' .

Let assume $w' = 0^k$, it follows that $c' = 0^n$ represents the null vector in the higher-dimensional space. Since $n > k$, we can establish a \mathbb{R}^{k+1} dimensional subspace. This subspace consists of k -dimension hyperplanes with $c' = 0^k$ serving as their origin. The reduced codeword \hat{c} that is the furthest from $c' = 0^k$ can be identified by selecting the k largest absolute outputs from the original codeword c , i.e., the Euclidean distance $d(\hat{c}, 0)$ is maximum. These outputs, in conjunction with their corresponding hash functions, form the reduced matrix \hat{G} .

Decoding via Hamming Distance Measurement: Leverage this methodology, we are equipped to compute the worst-case Hamming distance $\hat{x} = d_H(\hat{c}, \hat{c}') = k$ between an arbitrary random \hat{c} with respect to any non-zero codeword \hat{c}' . This calculation is made feasible following the application of the quantization process to the reduced codewords with $\text{sgn}(\cdot)$ function. If a worst-case Hamming distance $\hat{x} = d_H(\hat{c}, \hat{c}') = k$ exists, it signifies a unique instance among $\binom{n}{k}$ possible outcomes of a Hamming distance solution between the original n dimensional codeword, i.e., $x = d_H(c, c') = k$, that aligns with the expression given by Eq. 11.

Under these circumstances, a solution must exist for the angular difference $\theta\pi$ between the feature sample w and w' . This can be represented as:

$$\theta = \frac{\sum_i^k \text{sgn}(\hat{h}_i(w)) \neq \text{sgn}(\hat{h}_i(w'))}{n} = \frac{\arccos(w \cdot w')}{\pi} = k/n.$$

Above derivation establishes the conclusion that $\theta = \theta_0 = k/n$ with respect to the mean of the standard normal distribution, in accordance with the CLT:

$$\begin{aligned} d_H(\hat{c}, \hat{c}') - n\theta &= d_H(c, c') - n\theta_0 = 0 \\ \Rightarrow \theta_0 &= \theta = k/n. \end{aligned} \quad (12)$$

Such computation yields non-trivial null solutions (the zero) that satisfies our previous assumption, specifically manifesting as $w' = 0^k$, $\hat{c}' = 0^k$ and $c' = 0^n$. These null solutions are observed within the Euclidean space spanning multiple dimensions if and only if $\theta_0 = \theta = k/n$. Consequently, the densities corresponds to θ_0 and θ can therefore have their ratio complies with Eq. 8. This alignment provides us with the minimum solution for the negative log likelihood equivalent to the binary entropy function $nH_2(k/n)$ as described in Eq. 10.

It's worth noting that the null (zero) vector, i.e., 0^k and 0^n presents a unique special case in above derivation. The angular difference between the null vector ($w' = 0^k$) and any non-zero w can be measured as $\cos(\theta\pi) = w \cdot w' / (||w|| ||w'||)$, which is undefined due to the division by zero magnitude of the null vector. Despite this, we often assign a value of $\theta = k/n = 1/2$ by convention which signifies that a null vector is maximally dissimilar from any non-zero w , implying a scenario of maximum entropy ($nH_2(1/2) = n$). Conversely, for any pair of non-zero feature samples w and w' , if they are orthogonal (angle between them is 90 degrees), their entropy is also maximum, but for a different reason - their dissimilarity stems from having entirely different directions.

A 3-D Spacetime Interpretation: To better visualize and understand this process, we adopt a geometrical interpretation, represented in Figure 1. This illustration demonstrates the influence of three successive encoding stages: from $t = 1$ to $t = 3$. Although our model can easily extend to higher dimensions, including a \mathbb{R}^{k+1} subspace for arbitrary large n and $k < n$, for ease of visualization, we only focus on scenarios where $k = 2$, considering a 2-D space. In this context, the \mathbb{R}^{k+1} subspace contains maximum $t = 3$ unique hyperplanes. Each of these corresponds to a new solution of $w' = 0^k$ describing its largest distance with w along the additional dimension-the temporal axis. Each new encoding introduces a fresh hyperplane, collectively giving rise to a 3-D spacetime representation.

Model's Efficiency: Note that despite the fact that there is an exponential growth in entanglement complexity as delineated in Eq. 9, the intrinsic encoding and decoding process remains computationally efficient. Specifically, the resultant reduced codewords, (\hat{c} and \hat{c}') manifest quadratic time computational complexity, denoted as $O(n^2t)$ (see Algorithm 1 and 2 for asymptotic large n). This insight provides a crucial perspective on the design criteria for algorithms. Any algorithm intended to facilitate the realization of entanglement must be *efficient* enough to accommodate

computational demands that increase on an exponential scale with entanglement complexity. Figure 2 illustrates a toy example on how Algorithm 1 operates at $t = 1, 2, 3$ to produce reduced matrices $\{\hat{G}_1, \hat{G}_2, \hat{G}_3\}$ and their corresponding reduced codewords $\{\hat{c}_1, \hat{c}_2, \hat{c}_3\}$.

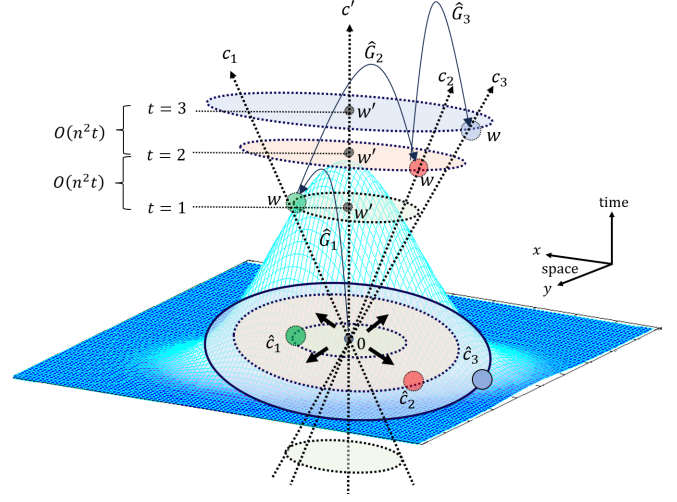


Fig. 1: The encoding process visually demonstrates the progressive divergence of w and w' , and their reduced codewords counterpart (\hat{c}, \hat{c}') with increasing encoding time step. We employ subscript notation to indicate that the reduced matrix \hat{G}_t corresponds to arbitrary encoding time steps $t = 1, t = 2$ and $t = 3$.

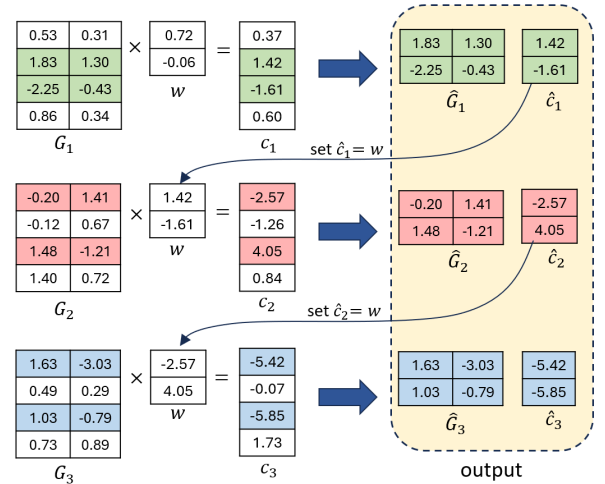


Fig. 2: Toy example demonstrates the encoding process with $t = 1, t = 2$, and $t = 3$. This process can be repeated for arbitrary large t .

4.2 Model's Completeness

Our analysis to this point has effectively confirmed the model's correctness guarantee in inferring θ_0 . Building on our earlier findings, it's natural to broaden our exploration to a multi-parameter context ($\theta_1, \dots, \theta_t$), described in Eq. 9.

The move to a multi-parameter setting is vital: for large values of n , the worst-case angular difference between w

and w' that can be computed is small, suggesting that the computable distance between them on a single unique hyperplane must also be small. This means that in order to compute larger distances between w and w' , we need to introduce additional iterations of encoding. As a result, computational complexity grows over time, correlating with the progression of entanglement.

When the encoding is applied recursively, i.e., using a new random generator function $G()$, and taking the reduced codeword as input feature samples, it produces new entanglement solution to the feature sample pair (w, w') corresponds to new parameter θ_i (for $i = 1, \dots, t$). These parameters collectively should adhere to the same conclusion presented in Eq. 12 due to their independent and identical characteristic, generally expressed as:

$$\theta_0 = \theta_1 = \dots = \theta_t = k/n.$$

Spacetime Expansion for the Preservation of Inertial Motion Frames: At each encoding time step, the introduction of randomness through new random reduced matrix (\hat{G}) may result in an inconsistent increase in the distance between the reduced codeword pair (\hat{c}, \hat{c}') . This variability result to w apparently undergoing acceleration away from w' at arbitrary random rates. To consistently apply classical physics laws in describing the relative motion between w and w' at each discrete encoding time step, particularly within an inertial frame of reference, it is imperative to uphold a constant angular difference in between (w, w') across distinct hyperplanes, as specified by our formulation $\theta_0 = \theta_1 = \dots = \theta_t = k/n$. The sole effective method for achieving this outcome is by adjusting their time intervals at each encoding time step. This adjustment precipitates a displacement of the spacetime origin away from hyperplanes characterized by greater distances between (w, w') , thereby giving rise to what we term “spacetime expansion.” The rationale for considering spacetime expansion becomes clear when we draw parallels with the well-known expansion of our universe [26], [27]. In our model, we emulate this cosmic expansion to establish entanglement, making it an intuitive way to explain the completeness of our model for parameter inference.

Drawing a parallel to the Einstein theory of special relativity [28], where all physical laws remain the same in every inertial reference frame, aforementioned approach also ensures a similar constancy. Specifically, with the condition that the angular difference between (w, w') remains consistent at each maximum encoding time step $t > 0$, it follows that the ratio of their Euclidean distance, represented as $d_t(w, w')$, to the corresponding time interval in seconds (s_t), denoted as $d_t(w, w')/s_t$, must remain invariant. This observation underscores the *principle of equivalence* in Einstein’s general theory of relativity, offering a foundational aspect to our model in characterizing the overall motion of w as it accelerates away from the non-inertial frame of w' . This accomplishment is made possible by employing distinct local inertial frames of reference, each associated with different maximum encoding time steps (t) through an entanglement process. As shown in Figure 4, at arbitrary $t > 0$, the angular difference between (w, w') represented as $\theta_1\pi = \theta_2\pi = \theta_3\pi$, remain constant. This constancy is concurrent with the expansion of spacetime, as the origin

progressively shifts away from the event hyperplane over time.

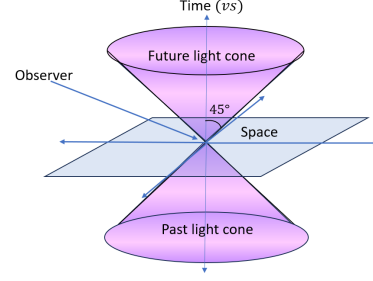


Fig. 3: The Minkowski’s spacetime diagram. v is the speed of light and s is unit of time (second).

Connection to Minkowski Spacetime: One can readily observe that the previously described geometric representation (see Figure 1 and 4) bear a strong resemblance to the Minkowski’s spacetime diagram (see Figure 3). More specific, when we treat (w, w') as distinct objects in physical context, our model posits that the ability to ascertain the existence of a solution for w deviates from w' with a maximum speed of $\frac{d_t(w, w')}{s_t} \leq v$, should not only be computationally feasible but also adhere to a specific computational complexity. This inequality holds because of $d_t(w, w')$ corresponds to maximum distance where their reduced codewords counterpart s.t. \hat{c} is furthest away from $\hat{c}' = 0^k$. This give us solution to the spacetime interval between two events always less than or equal to zero, as in $d_t(w, w')^2 - (vs_t)^2 \leq 0$. This scenario holds significance in Minkowski’s spacetime diagram. In particular, when we set v equal to the speed of light, events fall within the “light cone” in Minkowski’s spacetime diagram, known as the timelike region. This cone-shaped boundary defines the limits of causality and where information and physical effects can propagate.

Conversely, when $d_t(w, w')^2 - (vs_t)^2 > 0$ is the case, marking the region beyond the light cone, it is denoted as the spacelike area. In this spacelike region, events find themselves entirely devoid of any conceivable causal connection to the origin. Thus, an event occurring in the spacelike region is causally disconnected from the origin. No signal, even one moving at the speed of light, could reach from the origin to the spacelike event (or vice versa) without surpassing the speed of light.

The discovery above provides profound insights: despite our operation within a global non-inertial frame of reference wherein w undergoes acceleration away from w' , it becomes evident that every local inertial frame of reference, corresponding to distinct maximum encoding time steps (t), exists as an independent entity, and is computationally derivable. These frames of reference harmoniously adhere to the principles of Minkowski Spacetime. The fundamental tenet of the invariant speed of light within each local inertial frame, i.e., “locally Minkowskian,” thus remains steadfast and rigorously validated.

Put succinctly, while we witness an increases in computational complexity throughout the continuous encoding, we acquire valuable insights regarding their maximum spatial separation while still preserving a causal connection between them, thus upholding the *principle of locality*. This

leads us to consider a departure from Einstein’s postulate of special relativity, with a new emphasis on *increasing computational complexity as a fundamental principle*. Notably, this complexity surge stems from the second law of thermodynamics, which dictates entropy’s increases over time. To uphold information completeness and order within systems, the integration of computational entanglement emerges as an imperative necessity.

4.2.1 Introducing Computational Relativity: Time Dilation and Length Contraction

Having firmly established a profound connection between our model and the Minkowski spacetime, it is indeed valuable to delve deeper into Einstein’s special theory of relativity. This theoretical framework finds its most illustrative representation through the utilization of a Minkowski spacetime diagram, thoughtfully integrated with Lorentz transformations. This integrated approach provides invaluable insights into the effects of time dilation and length contraction within the realm of relativity.

Time Dilation: Without a preliminary examination of the Lorentz transformation, it is straightforward that, as elucidated in Figure 4, the continuous progression of entanglement over each encoding time step engenders a consequential expansion of spacetime. This expansion undeniably gives rise to increases in the temporal duration within every single local inertial frame of reference at relatively lower computational complexity, as exemplified by the increased in time interval $s_{t=1}$ to $s_{t'=1}$, and $s_{t=2}$ to $s_{t'=2}$ within the green and red cones in the figure respectively. This phenomenon plays a crucial role in ensuring the preservation of the invariance of the spacetime interval across all local inertial frames of reference at various computational complexities, as follows:

$$d_t(w, w')^2 - (vs_t)^2 = d_{t'}(w, w')^2 - (vs_{t'})^2,$$

for $t \geq t' > 0$.

Here, we refer to the scenario when $t = t'$, where v represents the maximum speed of light at maximum encoding time step t , corresponding to the frame of reference at lower complexity level (see Figure 4 for better visualization). In this context, frame of reference at greater complexity level demonstrates $d_{t'}(w, w') = d_t(w, w')$ (since $t = t'$). This frame of reference will undergo time dilation and exhibit a noticeable decrease in the angular difference between (w, w') due to spacetime expansion. Consequently, the measured speed $v_{t'} = d_{t'}(w, w')/s_{t'}$ at greater complexity level must decrease when compared with the maximum v , i.e., $v_{t'} < v$. Then, by describing $d_{t'}(w, w')^2 = (x_{t'})^2 + (y_{t'})^2$ with respect to $w' = 0^k$ as the origin for $k = 2$ -dimensions of space, representing a hyperplane in the 3-D spacetime; the most common form of the Lorentz transformation, parametrized by $v_{t'}$ confined to the x -direction, can be expressed as:

$$s_t = \gamma(s_{t'} - \frac{v_{t'}x_{t'}}{v^2}),$$

$$x_t = \gamma(x_{t'} - v_{t'}s_{t'}),$$

$$y_t = y_{t'},$$

with $\gamma = 1/\sqrt{1 - \frac{(v_{t'})^2}{v^2}}$ representing these Lorentz factor. Utilizing the Lorentz transformation equations, the changes

of time interval $(\Delta s_t, \Delta s_{t'})$ measured within local inertial frame of reference at particular encoding time steps $t = t'$ but different complexity level follows the time dilation formula:

$$\Delta s_{t'} = \frac{\Delta s_t}{\sqrt{1 - \frac{(v_{t'})^2}{v^2}}}.$$

This leads to the time appears to tick more slowly in higher complexity frame of reference.

Length Contraction: Given the aforementioned time dilation effect, the length contraction can be readily derived in similar way within the context when $t > t' > 0$. The length contraction formula is described as:

$$\Delta x_{t'} = \Delta x_t \sqrt{1 - \frac{(v_{t'})^2}{v^2}}.$$

This equation illustrates that the changes of length $\Delta x_{t'}$ along x -direction measured in reference frame of lower complexity level, relative to reference frame of higher complexity level (Δx_t) , appears to be contracted. The concept of length contraction becomes evident when we analyze Figure 4, by looking at the inner cone and extend it to a maximum encoding time step $t > t'$. For example, if we take $t = 2$ and $t' = 1$ then projecting the distance $d_{t'}(w, w')$ onto $t = 2$ while maintaining velocity at $v_{t'} < v$. This projected length is shorter than $d_t(w, w')$, which corresponds to the maximum speed of light v .

4.3 Comprehensive Role of Completeness and Correctness in Achieving Model Robustness Against Adversaries

In the context of adversarial robustness, when confronted with an arbitrary random query feature sample w' , a machine learning model needs, at the very least, the ability to recognize the existence of adversarial examples $w \in W$ within an arbitrary random feature sample distribution $W \in \mathbb{R}^k$. In this scenario, the encoding and decoding procedures developed with completeness guarantee over set of parameters $\theta_1, \dots, \theta_t$ become crucial for showcasing the possible existence of adversarial examples. These examples could exhibit identical angular difference despite the presence of large absolute distances within our formalized spacetime geometry (\mathbb{R}^{k+1}) .

As entanglement continue, corresponding to more encoding iterations, these adversarial examples display effects akin to time dilation and length contraction, with reductions in distances and angular differences relative to the reference frame of higher complexity. This makes it increasingly difficult for models positioned at a higher complexity to detect and differentiate their small differences. Consequently, this explains the adversarial conundrum: *Overparameterized machine learning models, as mentioned in [17], and those with heightened complexity [14], exhibit increased vulnerability to adversarial attacks. The enhanced complexity during training may effectively reduce the distance and angle between distinct features, such as ‘cat’ and ‘aircraft’, through entanglement processes. This can lead to misclassification and erroneous predictions.*

Specifically, our model posits that entanglement intrinsically corresponds to varying degrees of computational complexity distributed across distinct hyperplanes within

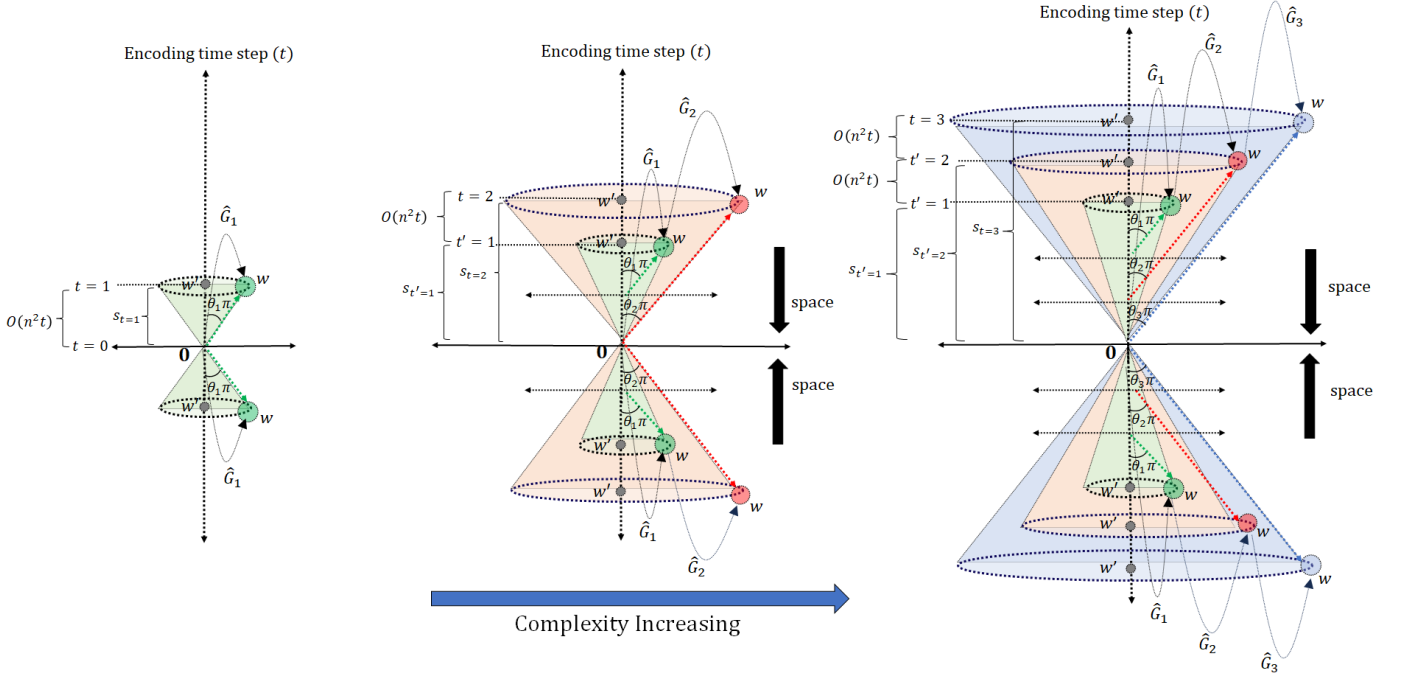


Fig. 4: A symmetrical behaviour influenced by continuous entanglement. When anchored to a common origin, for instance at $t = 0$, the angle between w and w' across individual local frames of reference increases with time, indicates it is accelerating. Yet, in the presence of entanglement, spacetime undergoes expansion. This results in every frame of reference (manifested at maximum encoding time step $t > t'$) being inertial, corresponds to different entanglement complexity levels.

spacetime. This underscores the idea that the complexity inherent in the entanglement process is indicative of the model's robustness in the face of adversarial examples. Without such a guarantee of model completeness that takes into account the spacetime interval with respect to complexity differences, the model would fail to ascertain the existence of adversarial examples, let alone formulate a strategy to combat them.

Above consideration is particularly relevant in situations where an arbitrary random encoder (analogue to an arbitrary random machine learning model) is utilized in the encoding or feature generation process for generating codewords $c \in \mathcal{C}$ distributed in an arbitrary random distributions over \mathbb{R}^n . In the worst-case scenario, these codewords may be closely clustered, possibly entangled due to deeply connected neuron-network layers, or possesses very small angular differences between them. Under these conditions, an arbitrary random decoder, without completeness guarantee, would face difficulty to distinguish between these codewords, leading to inevitable decoding errors.

Expanding on above rationale, we establish a significant relationship between the *existence* of a capable encoding/decoding scheme and entanglement, applicable to any arbitrary adversarial learning model. This relationship acts as a critical benchmark for those wishing to construct an optimal learning model, with the goal of achieving the best performance. Without a proper consideration on the model's construction and the relativistic effect of continuous entanglement, the model will lack the necessary completeness to encode and decode the codeword correctly to produce reliable predictive output.

This conclusion holds true even for those aiming to

create a model with a high degree of resilience against adversarial examples. When examining these adversarial examples from the vantage point of time dilation and length contraction, their intricate characteristics come to the forefront. This perspective implies that these examples are not mere outliers but instead emerge from situations where spacetime undergoes expansion, resulting in notable relativistic effects. Given this, guaranteeing the model's completeness and correctness in capturing and processing these relativistic effects becomes a fundamental prerequisite for achieving true adversarial robustness.

5 EXPERIMENTAL AND STIMULATION RESULTS

In this section, we undertake a comprehensive series of experiments and simulations designed to rigorously assess the intricacies of our model and validate its correctness and completeness. Algorithm 1 depict the Encoding procedure. Each encoding iteration produce a reduced codeword \hat{c} from input sample w and its corresponding reduced matrix \hat{G} that depends on the previous state.

We begin our investigative journey with biometric features. These distinctive and quantifiable human characteristics stand as keystones for personal identification, presenting an advanced shield compared to traditional authentication techniques. Amidst mounting concerns over cybersecurity and data integrity, it becomes imperative to dissect biometric features. This deep dive ensures resilience to potential adversarial onslaughts and amplifies their efficacy in tangible applications. Our spotlight narrows on three pivotal biometric modalities—fingerprint, face, and iris—which serve as representative input samples, denoted by w used for encoding and w' for decoding.

Algorithm 1

```

1: function Encoding( $w, n, t$ )
2:   Sample  $G \leftarrow \mathbb{R}^{n \times \ell}$   $\triangleright$  where  $\ell$  is the dimension of  $w$ 
3:   Compute  $c = Gw$ 
4:   Compute  $\hat{c} \leftarrow c$  and  $\hat{G} \leftarrow G$   $\triangleright$  This step compute
     the reduced codeword  $\hat{c}$  of dimension  $k < n$  from  $c$  s.t.
     the Euclidean distance  $d(\hat{c}, 0)$  is maximum, and return
     the  $k$ -rows of  $G$  that produce  $\hat{c}$ , i.e.,  $\hat{G}w = \hat{c}$ 
5:   Record  $\hat{c}$  and  $\hat{G}$ 
6:   set  $w = \hat{c}$ , and repeat Step 2 to Step 5 for  $t$  iterations.
7:   Output  $\{\hat{c}_1 \dots, \hat{c}_t\}$  and  $\{\hat{G}_1 \dots, \hat{G}_t\}$ 
8: end function

```

For fingerprints, we make use of a 99-dimensional feature, which is derived from fingerprint minutiae as proposed by Jin et al. [29]. The procedure involves generating the minutia cylinder-code using the MCC SDK [30], followed by a transformation through kernel principal component analysis (KPCA). For our data sources, we engage the FVC 2002 (subset DB1) and FVC 2004 (subset DB1) [31] datasets. Combined, these datasets offer 800 fingerprints (distributed as 100 sets with 8 fingerprints each). Following the FVC protocol [32], our study yielded 2,800 intra-class distance (genuine) scores and 4,950 inter-class distance (imposter) scores.

For face, we adopted the MagFace model [33], a pre-established CNN model. This model facilitates the creation of universal face feature embeddings with an input measurement (w, w') that possesses a dimensionality of 512. The datasets employed for this assessment include LFW [34] and CMU-PIE [35]. Specifically, with LFW, we strictly adhere to the 1:1 verification protocol which produces 3,000 genuine and an equivalent number of imposter test scores. In contrast, our utilization of CMU-PIE, in compliance with the FVC protocol, has yielded 18,768 intra-class and 2,278 inter-class distance scores.

For iris, we adopted the Iriscode technique, enhanced with a bloom filter as detailed by Rathgeb et al. [36]. This method is notable for its versatility: the Iriscode's distribution (specifically, the count of zeros and ones) can be adjusted by altering parameters L and W , which modulate the size of the bloom filter. Such adaptability offers a pathway to probe our model across varied distributions. Our primary dataset for this category is the CASIA database v3-interval [37]. It contains 2,639 iris images sourced from 396 individual subjects. The intra-class comparisons, where each iris template is cross-referenced with different samples from the same subject, amount to 4,406 inter-class distance scores. On the other hand, inter-class comparisons pair each template with the primary iris sample template from varying subjects, resulting in 199,110 inter-class distance scores.

5.1 Result 1: Entropy Reduced and Pronounced Time Dilation with Increment of Complexity

Algorithm 2 illustrates the Decoding algorithm employed in our initial experiment, which decodes by assessing the Hamming distance between the reduced codeword pair $(d_H(\hat{c}_t, \hat{c}'_t)/k)$ at maximum encoding time step t . The distances are measured from both inter-class and intra-class

comparisons and are illustrated in Figures 5-10, encompassing various configurations of (n, k) under same group of features samples we have used for face biometric.

Given sufficiently large t , both inter-class and intra-class distance distributions trend deviate toward the edges of the graph. Such behaviour provides compelling evidence of ongoing entanglement, which effectively reduces the the angular difference between every feature sample pair (w, w') .

As the measured distance between all reduced codeword pairs approach the graph's edge at $d_H(\hat{c}_t, \hat{c}'_t)/k = 1$, we obtain a solution where $\theta_0 = \dots = \theta_t = k/n$, where the entropy of the system is minimized to zero. The conclusion holds even when $d_H(\hat{c}_t, \hat{c}'_t)/k = 0$. This is because changing the sign of each bit in the reduced codeword \hat{c}_t (e.g., transitioning from -1 to 1 or vice versa) simply leads to the opposite outcome, emphasizing the symmetric entanglement result.

The decrease in the angular difference between (w, w') signifies time dilation, which becomes more pronounced for sample pairs that are closer together, i.e., the intra-class distance. This elucidates why the intra-class distance distribution tends to deviate towards the edges of the graph more rapidly (at smaller values of t). These distributions correspond to a lower complexity frame of reference at smaller encoding time steps.

It's essential to emphasize that these observed phenomena aren't limited to specific input samples (w, w') and their default distributions (see Figure 11-16). This effect is expected to be *universal*, entangling all feature sample pairs (w, w') with sufficiently large encoding iterations, regardless of their initial distance, feature type, or dataset.

Algorithm 2

```

1: function Decoding( $\{\hat{c}_1 \dots, \hat{c}_t\}, \{\hat{G}_1 \dots, \hat{G}_t\}, w'$ )
2:   for  $i = 1 : t$  do
3:     Compute  $\hat{c}'_i = \hat{G}_i w'$ 
4:     Set  $w' = \hat{c}'_i$ 
5:   end for
6:   Output  $d_H(\hat{c}_t, \hat{c}'_t)$ 
7: end function

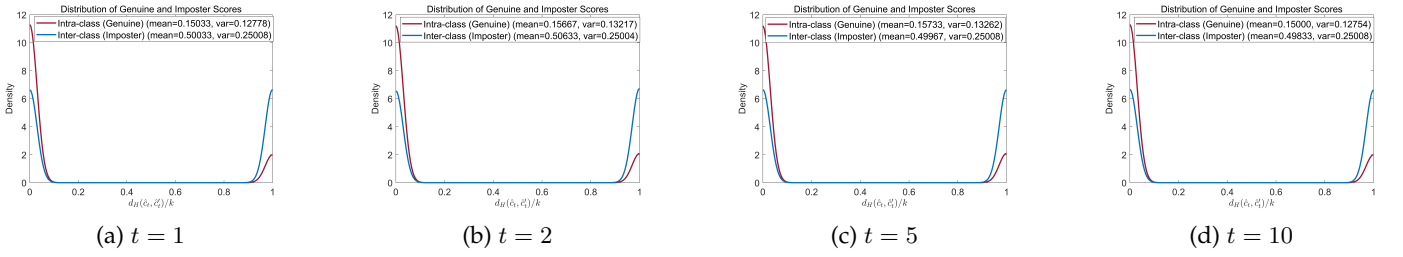
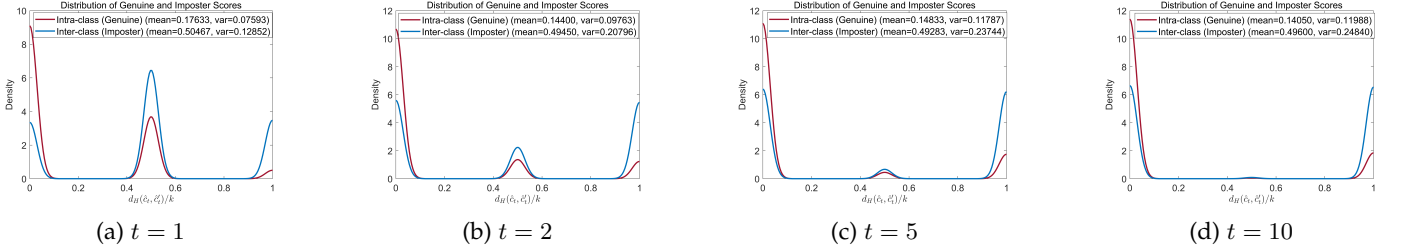
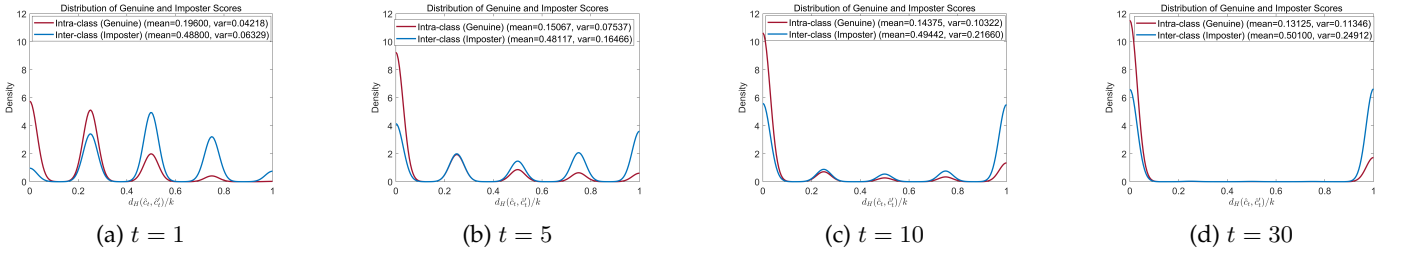
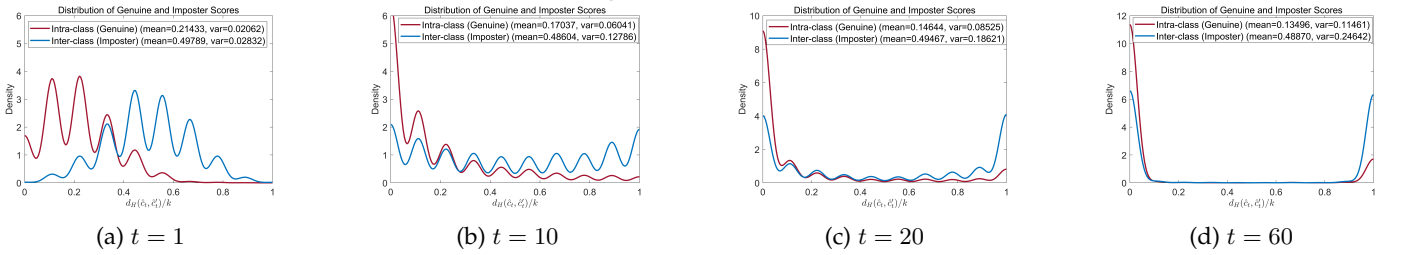
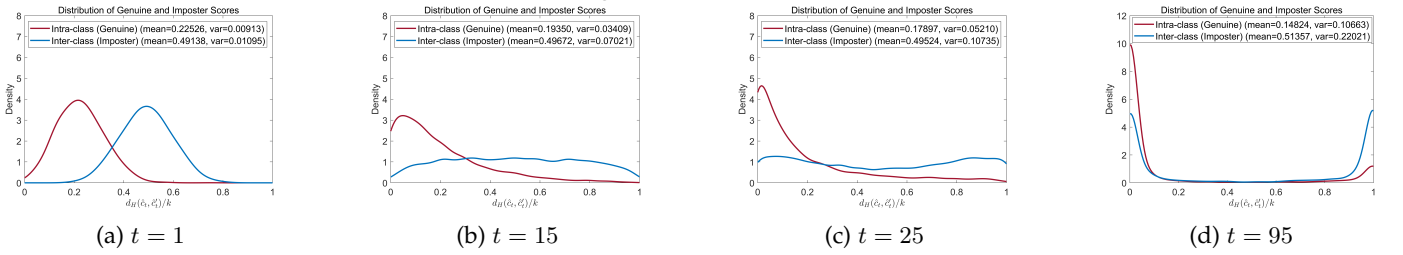
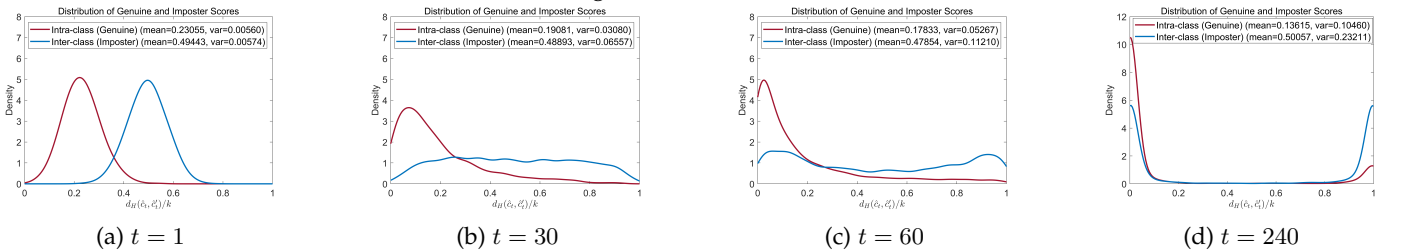
```

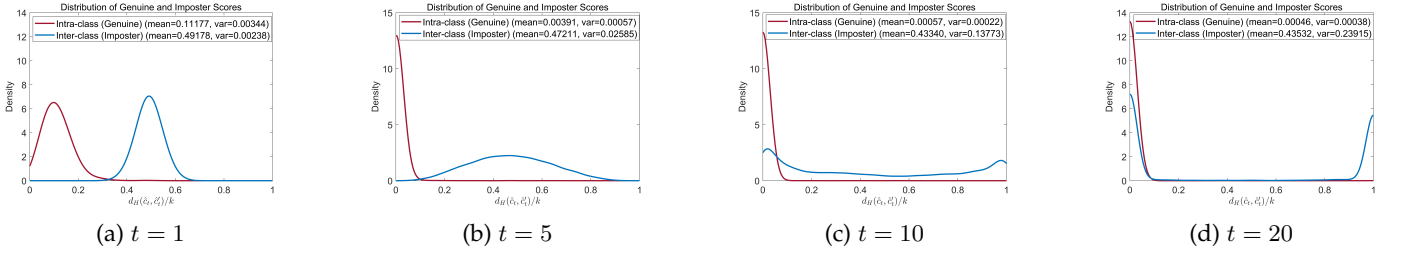
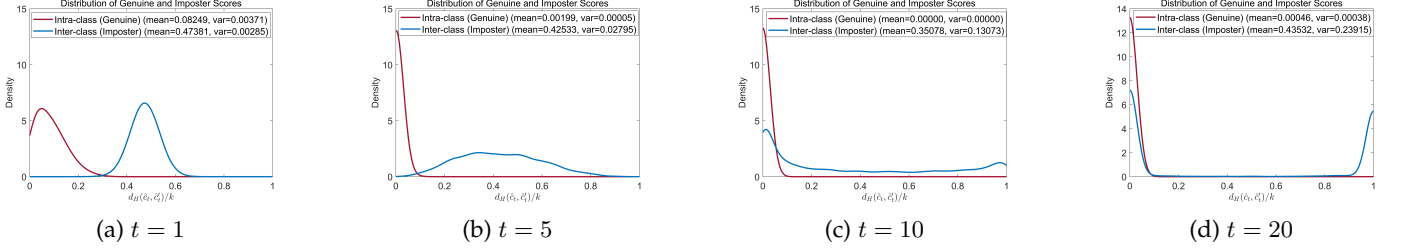
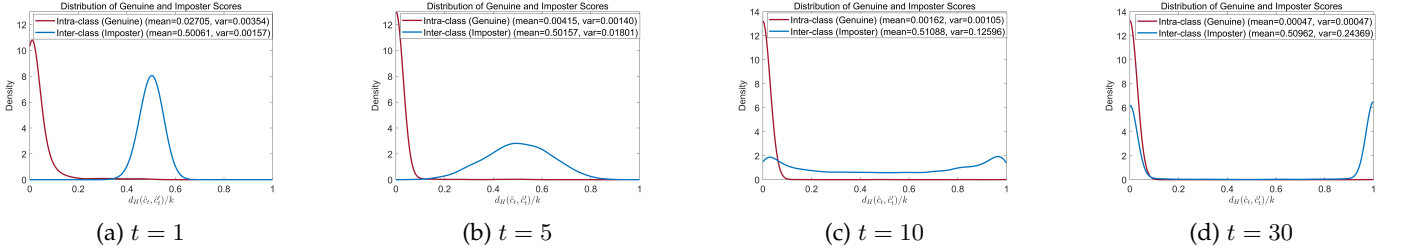
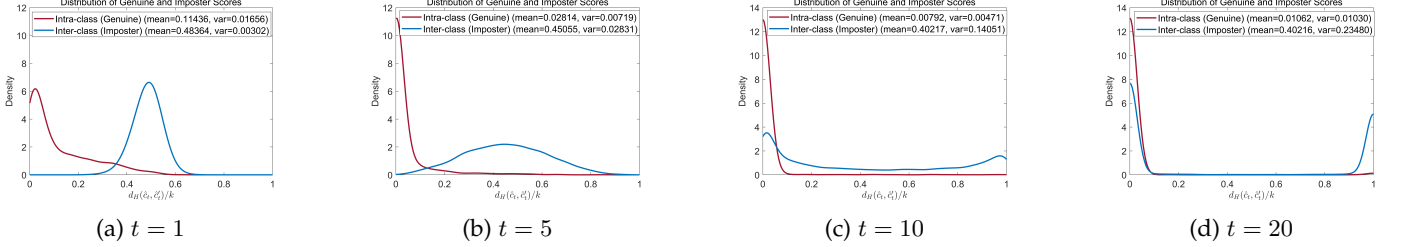
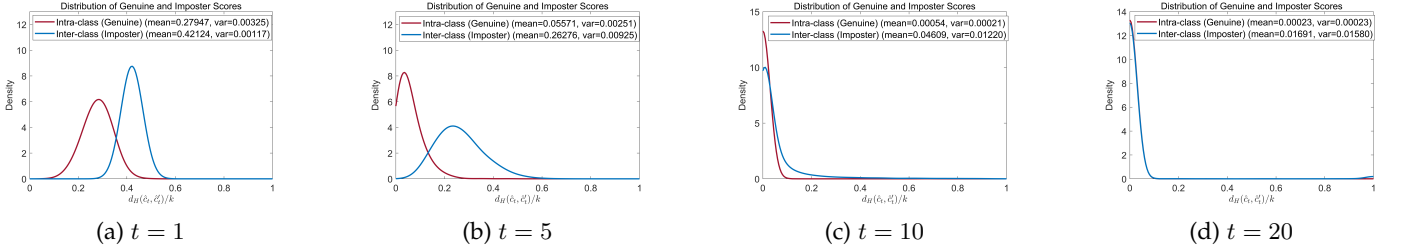
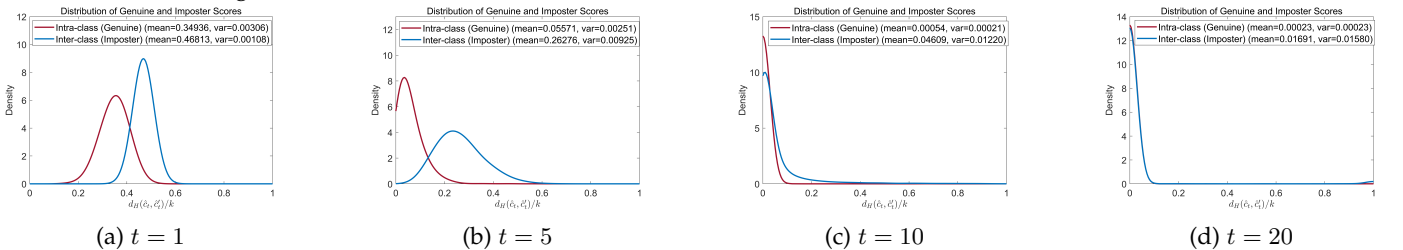
5.2 Result 2: Information Entangled In Quantized Context

In this section, we present experimental results demonstrating how information can exhibit entanglement in quantized context. This is important to note that the distinction of deterministic state about the absolute position and the angular difference, a.k.a entanglement angle, between (w, w') at particular maximum encoding time step $t > 0$, given the knowledge of the reduced matrices $\{\hat{G}_1, \dots, \hat{G}_t\}$, renders our model classically-defined, setting it apart from the quantum concept of entanglement.

In quantum mechanics [38], the entanglement of two spin-1/2 electrons is described probabilistically using the singlet state wave function:

$$|\Psi^-\rangle = \frac{1}{\sqrt{2}}(|-1\ 1\rangle - |1\ -1\rangle),$$

Fig. 5: $n = 2, k = 1$ Fig. 6: $n = 3, k = 2$ Fig. 7: $n = 5, k = 4$ Fig. 8: $n = 10, k = 9$ Fig. 9: $n = 25, k = 24$ Fig. 10: $n = 50, k = 49$

Fig. 11: $n = 500, k = 250$, LFW (Face)Fig. 12: $n = 500, k = 250$, CMUPE (Face)Fig. 13: $n = 500, k = 250$, FVC2002DB1 (Fingerprint)Fig. 14: $n = 500, k = 250$, FVC2004DB1 (Fingerprint)Fig. 15: $n = 500, k = 250$, with Bloom filter ($L = 7, W = 32$), CASIAv3-Interval (Iris)Fig. 16: $n = 500, k = 250$, with Bloom filter ($L = 9, W = 32$), CASIAv3-Interval (Iris)

with -1 and 1 denoting spin orientations. In this state, each electron exists in a superposition of both spin orientations until measured. When measured, the wave function collapses, leading to either the state $|-1\ 1\rangle$ or $|1\ -1\rangle$. This results in opposite spins, ensuring a total spin of zero due to their intrinsic correlation.

In our context, we focus on information related to the entanglement of entities, specifically their entanglement angle (characterized by parameters (n, k)) rather than their absolute positions in Euclidean space. When defining computational entanglement classically, individual bits of the reduced codewords \hat{c} or \hat{c}' exhibit entanglement analogous to electron spin. With sufficiently large number of encoding iterations, this results in the Hamming distance measurement $d_H(\hat{c}, \hat{c}') = k$ exhibit opposite states. For example, when $\hat{c} = (-1\ 1)$, it necessitates that $\hat{c}' = (1\ -1)$. This illustrates a strong correlation between the features, akin to the entanglement in quantum realm, with a total “spin” (represented in bits) sum to zero. Alternatively, a null solution can be achieved, resulting in entangled codewords always aligning in the same direction. This phenomena has been demonstrated in our second experiment, which employed Algorithm 3 to monitor the value of each individual bit value following the quantization of the reduced codeword pair over successive encoding iterations.

In our experiment, we selected parameters $n = 30$ and $t = 50$ with dimensions $k = 1$ (1-D), $k = 2$ (2-D) and $k = 3$ (3-D). These choices facilitated a more lucid visualization of the value shifts within the 1-D up to 3-D Euclidean spaces. Figure 17 illustrates the full spectrum of potential values, illuminating the trajectories through which the reduced codewords traverse the Euclidean domain. As anticipated, since the codewords undergo quantization—resulting in discrete outcomes of either -1 or 1 for each reduced codeword of dimension k —the findings presented in Figure 17 reinforce the notion that the quantized information naturally corresponds to its classical analogue within the Euclidean Space, visualized as a hypercube of dimension k .

Algorithm 3

```

1: function TracePath1( $\{\hat{c}_1 \dots, \hat{c}_t\}, \{\hat{G}_1 \dots, \hat{G}_t\}, w')$ 
2:   for  $i = 1 : t$  do
3:     Compute  $\hat{c}'_i = \hat{G}_i w'$ 
4:     Set  $\text{string}_1 = \text{sgn}(\hat{c}_i)$ 
5:     Set  $\text{string}_2 = \text{sgn}(\hat{c}'_i)$ 
6:     Record their quantized state after each quantization as  $p_i = (\text{string}_1, \text{string}_2)$ 
7:   end for
8:   Plot and trace the path for  $p_1, \dots, p_t$ 
9: end function

```

5.3 Result 3: Causality Behind Entanglement

In this section, we aim to shed light on the local aspects of entanglement within spacetime and delve into the underlying causality behind its formation. It's crucial to clarify our specific use of the term “locality” in this context to avoid any confusion. We are primarily concerned with the local realization of the processes that lead to the creation of entangled states. This concept of locality implies that any

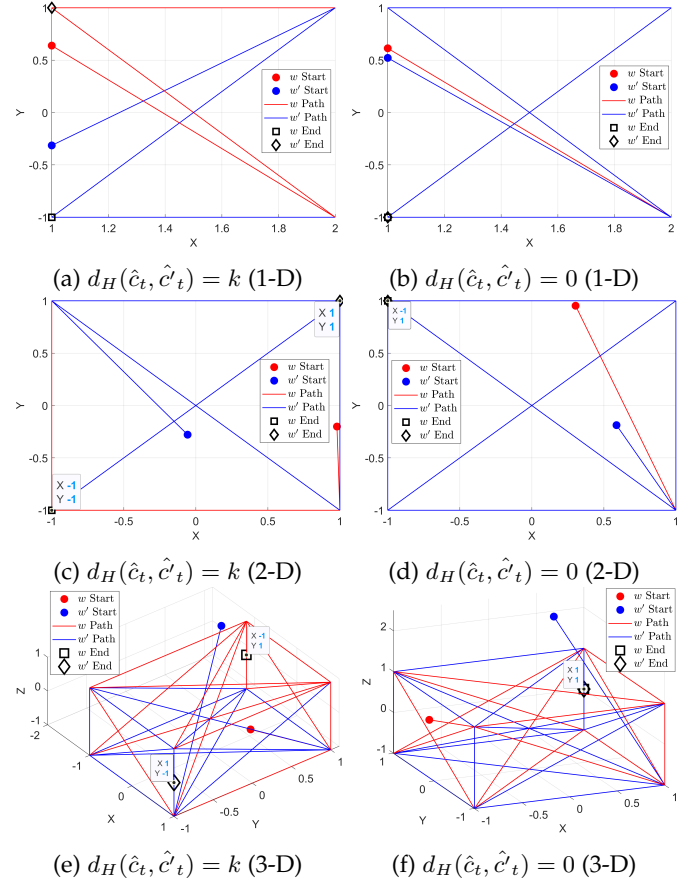


Fig. 17: After numerous encoding iterations, w and w' — represented by the entangled reduced codeword counterpart (\hat{c}, \hat{c}') — have *higher tendency* (around 80%) of exhibiting post-quantization positions within Euclidean Space with a Hamming distance of k (given the angle between w and w' is greater than $\pi/2$) or 0 (given the angle between w and w' is less than $\pi/2$).

event of entanglement occurs within the light cone region, where causal connections can be established between any sampled feature pair (w, w') .

While in quantum entanglement, it has been consistently observed that such principle of locality violated in the form of Bell’s inequality [39]–[42], implying that maintaining local causality requires violation of statistical independence between the choice of measurements and any hidden variables. In contrast, our emphasis on the intrinsic processes driving the emergence of entangled states highlights their statistical dependence on the reduced matrices $\{\hat{G}_1, \dots, \hat{G}_t\}$. This perspective provides a distinct approach to understanding entanglement, where the very nature of entanglement is rooted in these matrices and their statistical relationships putting it possible explanation of such violation.

It’s worth noting that there’s a common interpretation suggesting that violations of statistical independence imply the need for intricate, orchestrated correlations (fine-tuning or conspiracy) between hidden variables and measurement settings [43]. Such precise coordination is believed to be necessary to replicate entanglement correlations, a requirement that is often viewed as unlikely or contrived. However, we

contend that our introduction of statistical dependence in demonstrating entanglement through $\{\hat{G}_1, \dots, \hat{G}_t\}$ does not require fine-tuning, as shown in Result 1. This argument holds independently of system parameters (n, k) . The emergence of entanglement can be observed among arbitrary random feature pairs (w, w') , even if they start orthogonal, provided that t is sufficiently large. Recent work by Jonte et al. [44] shall lend support to this perspective. They propose redefining the physical state space and introducing a non-trivial measure, known as a “supermeasure,” where quantum correlations are intrinsic to the state space itself, rather than depending on hidden variable-measurement correlations [44]. In our case, we achieve these entanglement correlations using Cosine-distance based LSH for arbitrary random experiment settings and input feature samples.

Building upon our foundational analysis, we leveraged Algorithm 4 for our third experiment. Our goal was to meticulously trace the trajectory of the reduced codeword pair (\hat{c}, \hat{c}') within each encoding iteration. For the seek of information completeness, we bypass the quantization of the reduced codewords, retaining their continuous values within the Euclidean space. It then becomes essential to normalize these values at each encoding iteration. Such normalization safeguards the computational stability, especially preventing outcomes from diverging unboundedly. This safeguard is particularly crucial when envisioning scenarios where infinite encoding iterations could, in principle, cause w to deviates indefinitely from w' .

Our preliminary observations revealed something profound. At lower encoding iterations (i.e., smaller t), such as 2 or 5, the pathways of the reduced codeword pair appeared to lack discernible order, behaving ostensibly at random. However, a fascinating transition became evident as we incrementally increased the encoding iterations. The trajectories began to conform to distinct patterns, reminiscent of the properties of entanglement observed in the discrete domain. This was particularly astonishing given the fact that we were working within a continuous Euclidean spacetime. This emergence of structured behaviour, even in the absence of quantization, signified that the reduced codewords were not just randomly drifting but instead were adhering to the principles of entanglement in quantized context. Notably, they eventually entangled, displayed either opposite signs that summed to zero or aligned signs and magnitudes, leading them to converge at a singular endpoint given sufficiently large computational complexity.

In light of each encoding iteration, our observations, aligned with our interpretation, strongly hint that the very act of entanglement is an inherently local process. This localization seems to be guided and modulated by the specified reduced matrices $\{\hat{G}_1, \dots, \hat{G}_t\}$. What was initially perceived as random behaviour gives way to discernible patterns as the encoding progresses to a certain complexity level. This observation contradicts the principles of quantum entanglement, which describe entangled entities as initially existing in a superposition state that collapses upon measurement, often referred to as the ‘spooky action at a distance’ phenomenon [45].

Remarkably, while some may argue that our definition of computational entanglement might not directly correspond to entanglement in the quantum realm—a point we

acknowledge requires further theoretical and experimental justification using real quantum qubit—it’s crucial to recognize the substantial parallels within our model. Here, we efficiently establish strong correlations through algorithmic computation, both within quantized and non-quantized contexts. These correlations bear a striking resemblance to quantum entanglement in their ability to connect distant features. Dismissing this resemblance would mean missing the opportunity to explore the profound implications of computational entanglement. Specifically, in our case, given the statistical dependence inherent in the manifestation of entanglement within spacetime, it follows that the existence of non-local correlations can be precluded. Consequently, any system whose security relies on the presence of non-local correlations—implying the property of device independence (as discussed in [46]–[49]), might benefit from a thoughtful re-evaluation.

Algorithm 4

```

1: function TracePath2( $\{\hat{c}_1 \dots, \hat{c}_t\}, \{\hat{G}_1 \dots, \hat{G}_t\}, w')$ 
2:   for  $i = 1 : t$  do
3:     Compute  $\hat{c}'_i = \hat{G}_i w'$ 
4:     Set  $w' = \hat{c}'_i / \|\hat{c}'_i\|$  ▷ normalization take place here
5:     Set  $w = \hat{c}_i / \|\hat{c}_i\|$  ▷ normalization take place here
6:     Record their position as  $p_i = (w, w')$ 
7:   end for
8:   Plot and trace the path for  $p_1, \dots, p_t$ 
9: end function
```

5.4 Result 4: Pronounced Length Contraction with Increment of Complexity

In this subsection, we present a simulation demonstrating the phenomenon of length contraction across reference frames characterized by increasing complexity.

Noted that time dilation becomes evident as the angular difference between (w, w') decreases within each local frame of reference, so long as computational complexity continues to increase, i.e., during ongoing encoding with respect to $(t = t' > 0)$; length contraction is only observed when comparing different local frames of reference relative to their varying complexities, i.e., $t > t'$. In particular, while the ratio k/n remains constant throughout the entanglement process, its scale, denoted as $\lambda \cdot k/n$, should be increased to account for perspectives from a higher frame of reference. This adjustment ensures a consistent angular difference between (w, w) across all independent local frames of reference, as discussed earlier.

In light of this, we can reuse Algorithm 4, with arbitrary parameter choices. In this particular case, we have chosen $n = 30$ and $k = 2$ (for 2-D) or $k = 3$ (for 3-D), with increasing λ to demonstrate the length contraction effect from the perspective of increasing entanglement complexity. It is important to note that as k increases proportionally to n , the quantity of entangled information (in bits) also rises. However, due to the inherent limitations of human perception, visualizing dimensions greater than 3-D becomes challenging. For values of k exceeding three, we select only two and three random bit positions from the reduced codewords for 2-D and 3-D studies respectively. Hence, for $\lambda > 1$ in

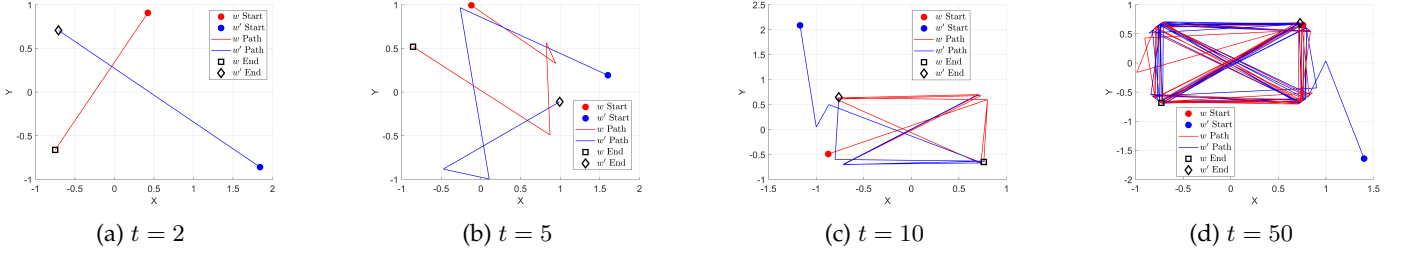


Fig. 18: $n = 30, k = 2, d_H(\hat{c}, \hat{c}') = k$, original angle between w, w' greater than $\pi/2$ (2-D)

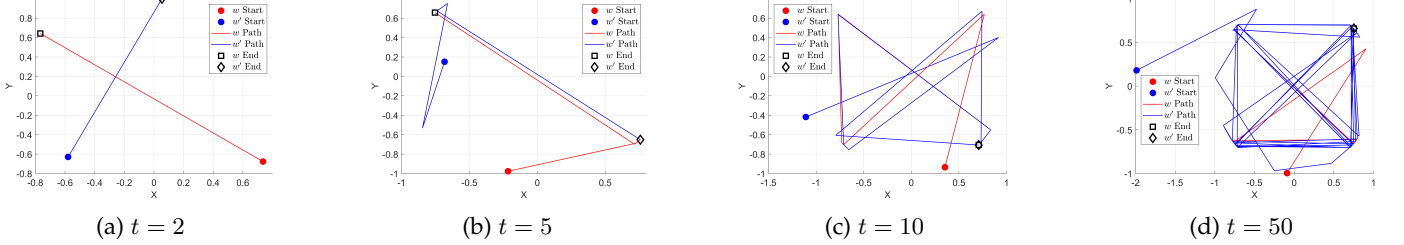


Fig. 19: $n = 30, k = 3, d_H(\hat{c}, \hat{c}') = 0$, original angle between w, w' less than $\pi/2$ (2-D)

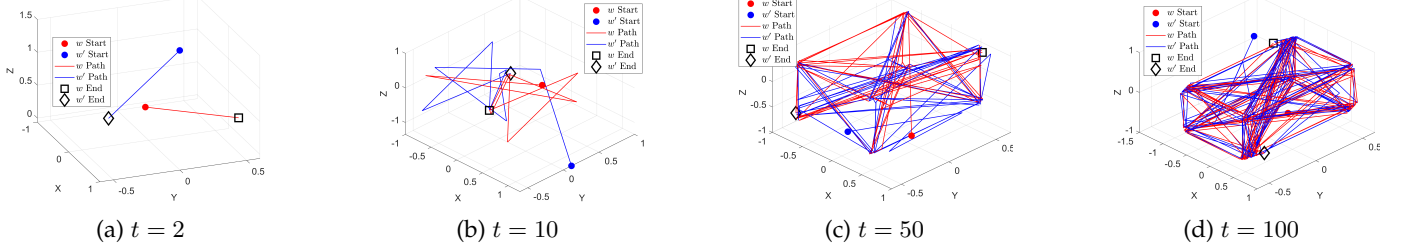


Fig. 20: $n = 30, k = 3, d_H(\hat{c}, \hat{c}') = k$, original angle between w, w' greater than $\pi/2$ (3-D)

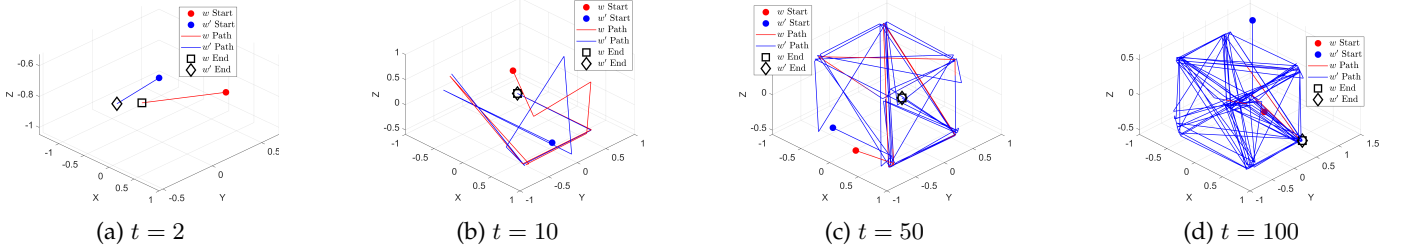


Fig. 21: $n = 30, k = 3, d_H(\hat{c}, \hat{c}') = 0$, original angle between w, w' less than $\pi/2$ (3-D)

these visualizations, information is lost as accurately representing their higher-dimensional flow necessitates tracing paths beyond three dimensions spacetime.

Figures 22-25 showcase the effects of increasing λ which indicates frames of reference with higher complexities. As evident from the visuals, when the complexity increases, the trajectory which the reduced codeword pair follows within the Euclidean space becomes more contracted. This results in the pair's motion appearing confined within a significantly smaller spatial region. Such an observation substantiates the premise that information traverses shorter distances when within frames of reference at greater complexity level.

6 MODEL APPLICATION

In this section, we delve into one potential application of computational entanglement, which facilitates reliable information transmission through information reconciliation [50]–[52]. Information reconciliation is a cryptographic

method that ensures Alice and Bob share a common secret after exchanging data over an unreliable channel, rectifying any errors and inconsistencies.

Common approaches to information reconciliation involve the use of error-correcting codes, such as linear codes [22]. These codes are mathematically well-defined and can correct errors efficiently for most practical purposes. However, the problem arises when considering the concept of *optimal decoding* [53].

In the context of error-correcting codes, optimal decoding involves determining the codeword from the codebook that is closest to the received data in some sense, typically measured using a suitable metric (e.g., Hamming distance for binary codes). However, in a worst-case scenario, all possible combinations of codewords and error patterns need to be considered, leading to an exponential growth in the search space.

To tackle the computational challenges associated with error correction, researchers have developed efficient algo-

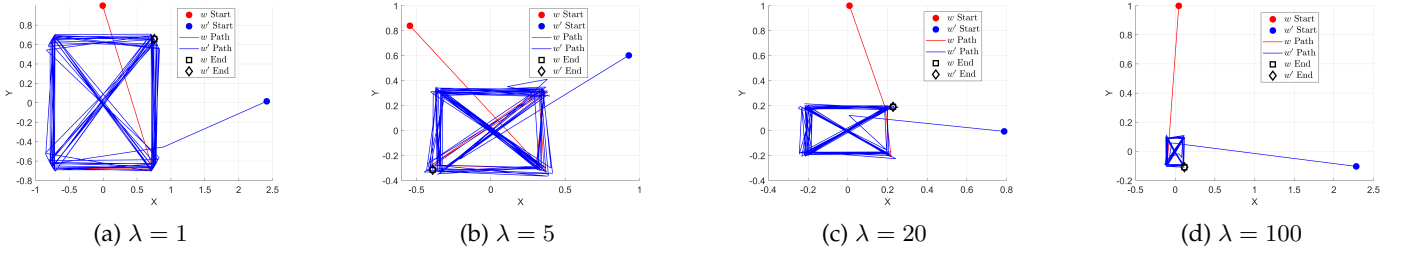


Fig. 22: $n = 30\lambda, k = 2\lambda, d_H(\hat{c}, \hat{c}') = 0$, original angle between w, w' less than $\pi/2$ (2-D)

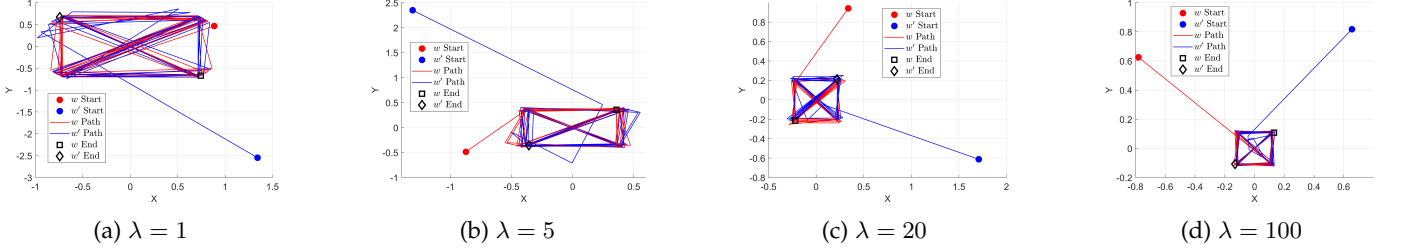


Fig. 23: $n = 30\lambda, k = 3\lambda, d_H(\hat{c}, \hat{c}') = k$, original angle between w, w' greater than $\pi/2$ (2-D)

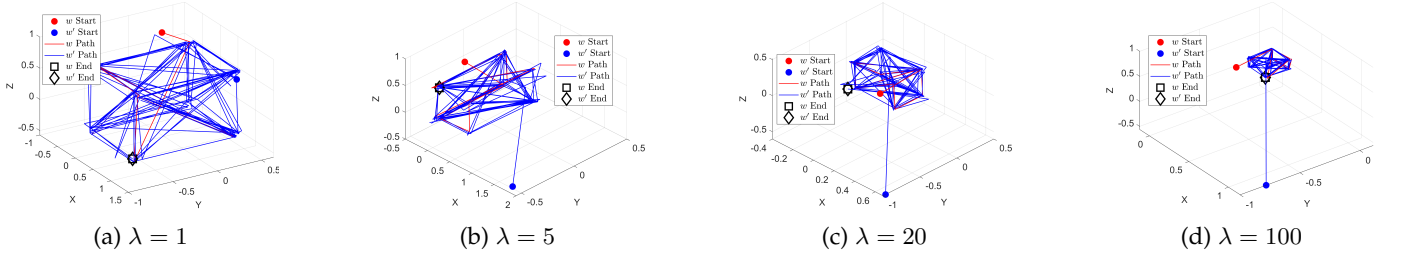


Fig. 24: $n = 30\lambda, k = 3\lambda, d_H(\hat{c}, \hat{c}') = 0$, original angle between w, w' less than $\pi/2$ (3-D)

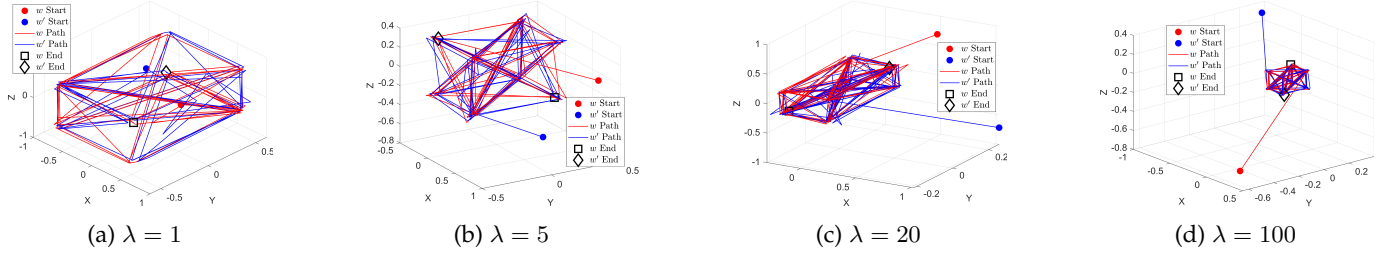


Fig. 25: $n = 30\lambda, k = 3\lambda, d_H(\hat{c}, \hat{c}') = k$, original angle between w, w' greater than $\pi/2$ (3-D)

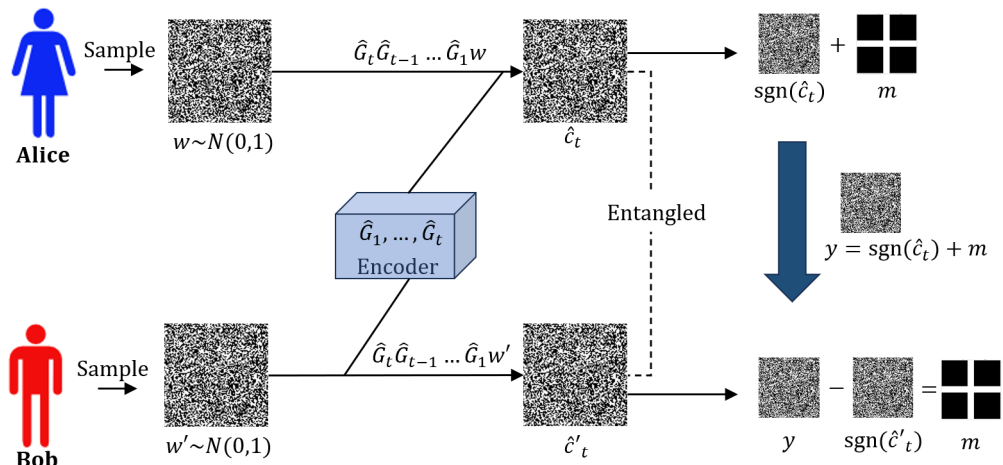


Fig. 27: Information reconciliation via computational entanglement

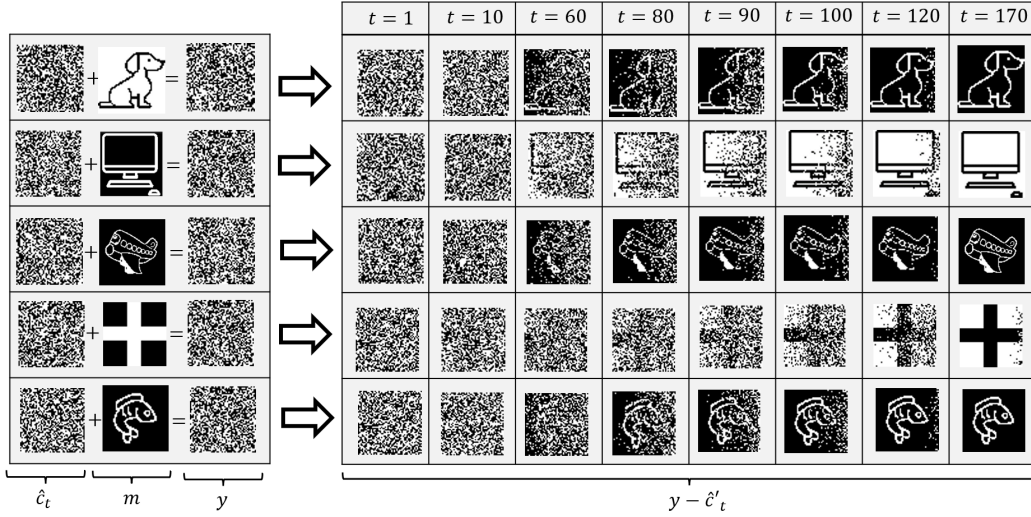


Fig. 28: In our toy example of information reconciliation, as t increases, entropy decreases due to ongoing entanglement. Time dilation and length contraction facilitate partial message recovery. When all bits of the reduced codeword (\hat{c}, \hat{c}') are fully entangled, perfect message recovery is achieved, and the system's entropy reaches a minimum of zero.

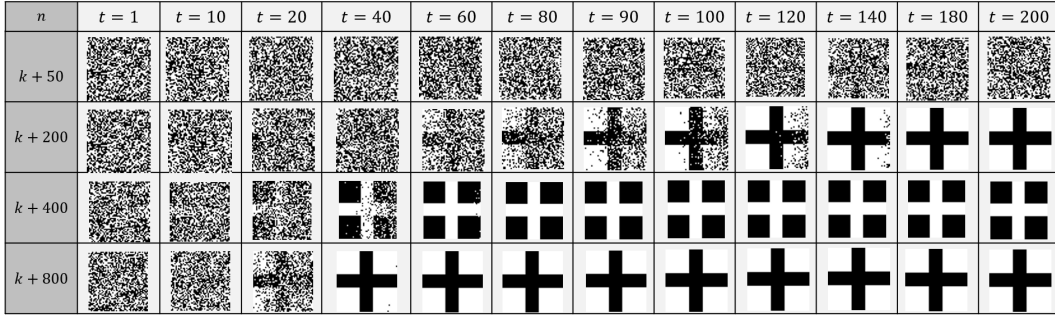


Fig. 29: Increase n lead to faster convergence for reduced codewords pair (\hat{c}, \hat{c}') to achieved fully entangled state, enable perfect recovery of the message at lower encoding time step t .

rithms, such as the Viterbi algorithm [54] for convolutional codes and belief propagation for LDPC codes [55]. These algorithms leverage mathematical techniques to streamline the search process and identify the most probable codeword without the need to exhaustively explore all possible options.

However, it's important to note that the complexity of the Viterbi algorithm increases exponentially with the constraint length, which is essentially the "memory" of the code. This is done to accommodate a higher degree of error correction. Similarly, belief propagation may demand more iterations for dependable decoding, and this can be influenced by various factors, including the structural characteristics of the code and the signal-to-noise ratio.

Furthermore, it's worth highlighting that finding the optimal decoding solution for arbitrary error correction codes presents a significant challenge. This problem falls under the category of NP (non-deterministic polynomial time)-hard problems [56]. In practical terms, this means that as the code's dimension and the number of errors to be corrected increase, the computational resources, both in terms of time and memory, required to achieve an exact solution grow exponentially.

6.1 Information Reconciliation via Computational Entanglement

Our proposed entanglement approach provides a deterministic and computationally efficient solution that circumvents the inherent NP-hardness associated with the maximum likelihood decoding problem. More precisely, it enables information reconciliation through computational entanglement, with a firm guarantee of optimizing the likelihood of the adversary's objective, as outlined in Eq. 10. Figure 27 illustrates an example of how entanglement can be applied to perform information reconciliation. In this context, we considered Alice and Bob, each independently sampling random features denoted as w and w' , respectively, following specific probability distributions, such as the standard normal distribution.

In the realm of computational entanglement, an intriguing possibility emerges: even if w and w' start as orthogonal entities, given the freedom to utilize an encoder associated with an expansive collection of reduction matrices, denoted as $\hat{G}_1, \dots, \hat{G}_t$; with a sufficiently large encoding time step t , Alice and Bob can collaboratively generate reduced codewords, \hat{c} and \hat{c}' , that possess entangled characteristics. These entangled codewords can subsequently serve as a means for encoding and decoding a message denoted as m , thus

facilitating information transmission between the parties involved.

To enhance the system’s resilience against errors, it is conceivable for Alice and Bob to extend the encoding process by increasing t . This expanded encoding process should eventually yield entangled reduced codeword pairs, represented as (\hat{c}, \hat{c}') . Upon successful generation of such an entangled pair, we observe that the Hamming distance $d_H(\hat{c}, \hat{c}')$, results in either k or 0 . Here, k signifies the number of bits in the entangled codeword pair. This outcome implies that any encoded message, denoted as

$$y = \text{sgn}(\hat{c}) + m,$$

is recoverable through the decoding process, follows

$$y - \text{sgn}(\hat{c}') = (\text{sgn}(\hat{c}) - \text{sgn}(\hat{c}')) + m,$$

leading to the recovered output to be either equal to m or $1^k - m$.

Nevertheless, it is essential to consider the reduction in entropy that occurs during continuous entanglement. Specifically, in the context of secure communication, the encoded message is susceptible to eavesdropping or malicious alteration by an active adversary. This reduction in entropy primarily stems from the studied relativistic effect, which diminishes the angular difference and distance between the input feature samples (w, w') .

In light of this, the choice of the maximum encoding time step t , should align with the maximum tolerable error, represented as the maximum Hamming distance, between the reduced codeword pair (\hat{c}, \hat{c}') . This decision is pivotal because maximum error correction entails the highest level of entropy loss. The maximum tolerable error is intricately linked to the angular difference between the input feature samples (w, w') .

This interplay results in an inherent information-theoretical trade-off between number of tolerable error and entropy loss, wherein the amount of information that an adversary can learn from intercepted messages y , is contingent upon the angular difference between the input feature sample (w, w') . Consequently, the best the adversary can hope to accomplish in this scenario is no more effective than Bob’s capability to decode the message y using any randomly chosen w' .

Toy Example: Figure 28 illustrates the outcomes of our practical application of computational entanglement for encoding arbitrary messages, represented as 50×50 binary images encompassing various objects like dogs, laptops, airplanes, crosses, and fish. The process involves the generation of reduced codeword pairs (\hat{c}, \hat{c}') from feature samples (w, w') , which are randomly drawn from a standard normal distribution. The encoded message appears initially as random and noisy.

As t increases, the entanglement process unfolds, leading to the emergence of relativistic effects such as time dilation and length contraction. The system entropy then continue to decreases. These effects ultimately entangled every bits of the reduced codeword pair (\hat{c}, \hat{c}') , enable the successful decoding of the message using \hat{c}' through the operation $y - \hat{c}'$, resulting in a perfect recovery of the original message.

As shown in Eq. 10, each encoding iteration incurs an entropy loss described as $nH_2(k/n)$. This entropy loss

signifies the maximum tolerable errors per encoding iteration. Increasing the parameter n accelerates the convergence of the reduced codeword pair (\hat{c}, \hat{c}') toward complete entangled state, i.e., every bits of the reduced codeword pair (\hat{c}, \hat{c}') are entangled. This outcome is evident in Figure 29, where an increase in n enables perfect message recovery at lower values of t . This underscores the redundancy principle in error correction code design: greater redundancy ($n > k$) allows for the correction of more errors but results in higher entropy loss.

6.2 Adversary Example Generation Through the Lens of Information Reconciliation

In continuation of our earlier discussion regarding the application of information reconciliation, we now embark on a deeper examination, shedding light on how this process can be harnessed to facilitate the generation of adversarial examples, thereby offering new insight for adversarial machine learning studies. Within this exploration, we revisit the previous scenario encompassing Alice and Bob’s information reconciliation process. However, we approach it from a fresh perspective, one that focuses on an adversarial context.

In this pursuit, we delve into a different scenario depicted in Figure 30. Here, we grant an adversary the capability to sample arbitrary random noise, denoted as w , which follows a standard normal distribution. In this intriguing context, the adversary is capable of creating a reduced codeword \hat{c} from w , through encoding. This reduced codeword, resemble random Gaussian noise, can exhibiting arbitrary variance parametrized by α . The adversary can generate an adversarial example, denoted as y , by injecting additive noise into the “Panda” sample (m), specifically by adding $\alpha\hat{c}$ to it, i.e., $y = \alpha\hat{c} + m$.

A noteworthy insight from our model strongly suggests that it is indeed possible to derive a corresponding reduced codeword, \hat{c}' , from an arbitrary random sample, which we’ll refer to as the “Gibbon” (w'). Consequently, \hat{c}' can be generated in a manner that inherently entangled with \hat{c} . This entangled relationship serves as the foundation for the effective reconciliation of the “Panda” information from the adversary example y , even in the presence of what might initially appear as an unrelated or uncorrelated “Gibbon” sample.

As part of our assessment, we employed images of “Gibbon” and “Panda,” each sized at 50×50 , and chose $n = k + 1000$ to expedite the attainment of a fully entangled state. In Figure 31, we observe the impact of increasing α on the original sample, resulting in the generation of the adversary example y . It becomes evident that higher levels of noise necessitate a greater number of iterations to successfully reconcile the original “Panda” sample from y , utilizing the “Gibbon” image.

In summary, through viewing adversary examples through the lens of information reconciliation, we gain deeper insights into their emergence via the intricate process of entanglement. This perspective allows us to appreciate how the entanglement of various data elements plays critical roles in machine learning models, not only in terms of understanding vulnerabilities but also in developing robust defenses and enhancing the resilience of these models against adversarial threats.

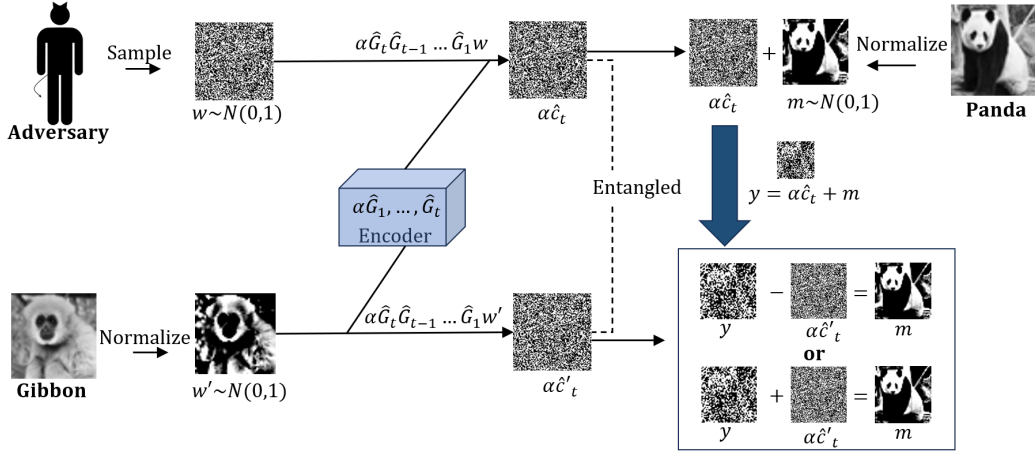


Fig. 30: Examining adversary example generation through the lens of information reconciliation.

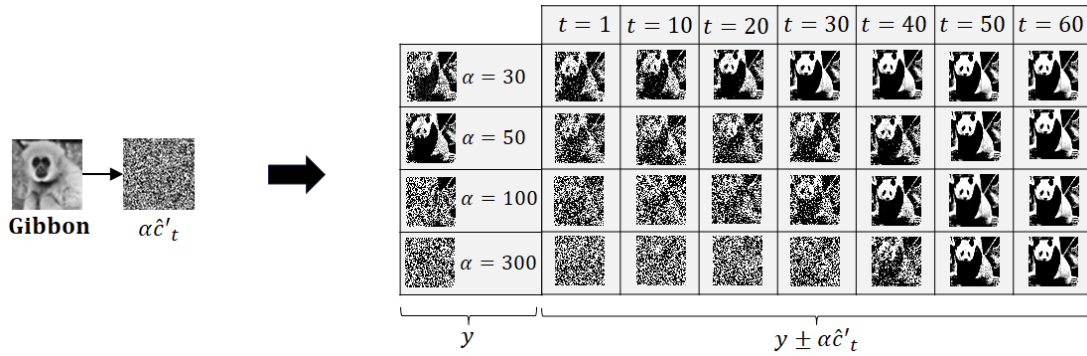


Fig. 31: Figure demonstrates that as α increases, it leads to greater perturbation on the original “Panda” sample. Consequently, a higher number of encoding iterations is required to successfully reconcile the original sample from the effects of the increasing noise level.

7 CONCLUSIVE STATEMENT

In this discourse, we have advanced a computational interpretation of the transferability phenomena in adversary machine learning through exploration of entanglement. Our perspective underscores that the tangible manifestations of entanglement is intrinsically local and computational in nature. Our insights have profound implications, particularly when considering feature samples subjected to relativistic effects like time dilation and length contraction. It’s imperative for the scientific community to intensify efforts to understand how existing machine learning models might adhere to the same laws of physics and potentially become entangled even when feature samples are distant.

Our revelation regarding computational entanglement is far from trivial and holds immense significance. It specifically suggests the intriguing possibility that even arbitrary random features, in principle, can become entangled and demonstrate adversarial properties when subjected to a sufficiently high level of complexity. In light of our findings, it is crucial for the machine learning community to exercise caution when prioritizing model accuracy through the adoption of increasingly complex and less interpretable models. Our research unequivocally showcases the existence of computational entanglement properties, strongly suggesting that even highly complex models, including

deep neural networks with intricate layer connections, may not be impervious to such entanglement effects. Remarkably, our model demonstrates entanglement with a minimal parameter count, as few as 60, and even fewer when analyzed within the context of maximum encoding time step t and high noise levels $\alpha = 300$ (refer to Figure 31). The existence of simpler model with profound consequences should not be overlooked or underestimated.

If there’s one thing our research has brought to light, it’s the emerging connection between the domains of computation and physics. By exploring the possibility that the fundamental laws of physics might be deeply intertwined with a computational framework, particularly in the context of entanglement, we inadvertently raise the idea that the Turing machine, known for its computational universality, could potentially simulate, or at the very least closely approximate, these intricate physical phenomena. This convergence of concepts not only hints at a shift in our understanding of the universe but also reaffirms that our current comprehension, rooted in the notion of computational entanglement, may represent just the surface of a much deeper conceptual landscape. As we venture further into this territory, it becomes increasingly crucial to differentiate between the intricacies of the model and the broader reality it seeks to capture.

Lastly, but certainly not least, while we have the freedom

to configure the reduced matrix set $\{\hat{G}_1, \dots, \hat{G}_t\}$ in various ways to promote entanglement among feature samples, what truly captivates us is the steadfast alignment of our results with the foundational deterministic principles of classical physics. This intriguing harmony, reminiscent of Einstein's timeless adage, 'God does not play dice,' inspires us to embark on a profound journey into the intricacies of determinism within the cosmos. It encourages us to delve deeper into profound questions about the nature of determinism in the universe, particularly how our choices, even when introducing randomness through these reduced matrices, interact with the deterministic essence that governs the physical world. This exploration provides an enticing pathway for further research, not limited to machine learning, but also at the intersection of determinism, free will and fundamental physics.

REFERENCES

- [1] N. Dalvi, P. Domingos, Mausam, S. Sanghai, and D. Verma, "Adversarial classification," in *Proceedings of the tenth ACM SIGKDD international conference on Knowledge discovery and data mining*, 2004, pp. 99–108.
- [2] D. Lowd and C. Meek, "Adversarial learning," in *Proceedings of the eleventh ACM SIGKDD international conference on Knowledge discovery in data mining*, 2005, pp. 641–647.
- [3] M. Barreno, B. Nelson, R. Sears, A. D. Joseph, and J. D. Tygar, "Can machine learning be secure?" in *Proceedings of the 2006 ACM Symposium on Information, computer and communications security*, 2006, pp. 16–25.
- [4] B. Biggio, B. Nelson, and P. Laskov, "Poisoning attacks against support vector machines," *arXiv preprint arXiv:1206.6389*, 2012.
- [5] C. Szegedy, W. Zaremba, I. Sutskever, J. Bruna, D. Erhan, I. Goodfellow, and R. Fergus, "Intriguing properties of neural networks," *arXiv preprint arXiv:1312.6199*, 2013.
- [6] I. J. Goodfellow, J. Shlens, and C. Szegedy, "Explaining and harnessing adversarial examples," *arXiv preprint arXiv:1412.6572*, 2014.
- [7] N. Papernot, P. McDaniel, and I. Goodfellow, "Transferability in machine learning: from phenomena to black-box attacks using adversarial samples," *arXiv preprint arXiv:1605.07277*, 2016.
- [8] J. Gilmer, L. Metz, F. Faghri, S. S. Schoenholz, M. Raghu, M. Wattenberg, and I. Goodfellow, "Adversarial spheres," *arXiv preprint arXiv:1801.02774*, 2018.
- [9] S. Bubeck, Y. T. Lee, E. Price, and I. Razenshteyn, "Adversarial examples from computational constraints," in *International Conference on Machine Learning*. PMLR, 2019, pp. 831–840.
- [10] A. Shafahi, W. R. Huang, C. Studer, S. Feizi, and T. Goldstein, "Are adversarial examples inevitable?" *arXiv preprint arXiv:1809.02104*, 2018.
- [11] A. Madry, A. Makelov, L. Schmidt, D. Tsipras, and A. Vladu, "Towards deep learning models resistant to adversarial attacks," *arXiv preprint arXiv:1706.06083*, 2017.
- [12] D. Stutz, M. Hein, and B. Schiele, "Disentangling adversarial robustness and generalization," in *Proceedings of the IEEE/CVF Conference on Computer Vision and Pattern Recognition*, 2019, pp. 6976–6987.
- [13] A. Ilyas, S. Santurkar, D. Tsipras, L. Engstrom, B. Tran, and A. Madry, "Adversarial examples are not bugs, they are features," *Advances in neural information processing systems*, vol. 32, 2019.
- [14] A. Demontis, M. Melis, M. Pintor, M. Jagielski, B. Biggio, A. Oprea, C. Nita-Rotaru, and F. Roli, "Why do adversarial attacks transfer? explaining transferability of evasion and poisoning attacks," in *28th USENIX Security Symposium (USENIX Security 19)*. Santa Clara, CA: USENIX Association, Aug. 2019, pp. 321–338. [Online]. Available: <https://www.usenix.org/conference/usenixsecurity19/presentation/demontis>
- [15] A. R. Brown and L. Susskind, "Second law of quantum complexity," *Physical Review D*, vol. 97, no. 8, p. 086015, 2018.
- [16] P. Domingos, "A few useful things to know about machine learning," *Communications of the ACM*, vol. 55, no. 10, pp. 78–87, 2012.
- [17] C. Zhang, S. Bengio, M. Hardt, B. Recht, and O. Vinyals, "Understanding deep learning (still) requires rethinking generalization," *Communications of the ACM*, vol. 64, no. 3, pp. 107–115, 2021.
- [18] R. Caruana, Y. Lou, J. Gehrke, P. Koch, M. Sturm, and N. Elhadad, "Intelligible models for healthcare: Predicting pneumonia risk and hospital 30-day readmission," in *Proceedings of the 21th ACM SIGKDD international conference on knowledge discovery and data mining*, 2015, pp. 1721–1730.
- [19] C. Rudin, "Stop explaining black box machine learning models for high stakes decisions and use interpretable models instead," *Nature machine intelligence*, vol. 1, no. 5, pp. 206–215, 2019.
- [20] U. Fayyad, G. Piatetsky-Shapiro, and P. Smyth, "From data mining to knowledge discovery in databases," *AI magazine*, vol. 17, no. 3, pp. 37–37, 1996.
- [21] U. Shafique and H. Kaiser, "A comparative study of data mining process models (kdd, crisp-dm and semma)," *International Journal of Innovation and Scientific Research*, vol. 12, no. 1, pp. 217–222, 2014.
- [22] E. Berlekamp, *Algebraic coding theory*. World Scientific, 1968.
- [23] B. Biggio and F. Roli, *Adversarial Machine Learning*. Springer, 2018.
- [24] N. Inkawhich, W. Wen, and H. H. Liu, "Understanding and enhancing the transferability of adversarial examples," *arXiv preprint arXiv:2007.03256*, 2020.
- [25] M. S. Charikar, "Similarity estimation techniques from rounding algorithms," in *Proceedings of the thirty-fourth annual ACM symposium on Theory of computing*, 2002, pp. 380–388.
- [26] E. Hubble, "A relation between distance and radial velocity among extra-galactic nebulae," *Proceedings of the national academy of sciences*, vol. 15, no. 3, pp. 168–173, 1929.
- [27] L. Guzzo, M. Pierleoni, B. Meneux, E. Branchini, O. Le Fèvre, C. Marinoni, B. Garilli, J. Blaizot, G. De Lucia, A. Pollo *et al.*, "A test of the nature of cosmic acceleration using galaxy redshift distortions," *Nature*, vol. 451, no. 7178, pp. 541–544, 2008.
- [28] A. Einstein *et al.*, "On the electrodynamics of moving bodies," *Annalen der physik*, vol. 17, no. 10, pp. 891–921, 1905.
- [29] Z. Jin, M.-H. Lim, A. B. J. Teoh, B.-M. Goi, and Y. H. Tay, "Generating fixed-length representation from minutiae using kernel methods for fingerprint authentication," *IEEE Transactions on Systems, Man, and Cybernetics: Systems*, vol. 46, no. 10, pp. 1415–1428, 2016.
- [30] R. Cappelli, M. Ferrara, and D. Maltoni, "Minutia cylinder-code: A new representation and matching technique for fingerprint recognition," *IEEE transactions on pattern analysis and machine intelligence*, vol. 32, no. 12, pp. 2128–2141, 2010.
- [31] D. Maio, D. Maltoni, R. Cappelli, J. L. Wayman, and A. K. Jain, "Fvc2004: Third fingerprint verification competition," in *International conference on biometric authentication*. Springer, 2004, pp. 1–7.
- [32] —, "Fvc2002: Second fingerprint verification competition," in *Object recognition supported by user interaction for service robots*, vol. 3. IEEE, 2002, pp. 811–814.
- [33] Q. Meng, S. Zhao, Z. Huang, and F. Zhou, "Magface: A universal representation for face recognition and quality assessment," in *Proceedings of the IEEE/CVF Conference on Computer Vision and Pattern Recognition*, 2021, pp. 14 225–14 234.
- [34] G. B. Huang, M. Mattar, T. Berg, and E. Learned-Miller, "Labeled faces in the wild: A database for studying face recognition in unconstrained environments," in *Workshop on faces in Real-Life Images: detection, alignment, and recognition*, 2008.
- [35] T. Sim, S. Baker, and M. Bsat, "The cmu pose, illumination, and expression (pie) database," in *Proceedings of fifth IEEE international conference on automatic face gesture recognition*. IEEE, 2002, pp. 53–58.
- [36] C. Rathgeb, F. Breiting, and C. Busch, "Alignment-free cancelable iris biometric templates based on adaptive bloom filters," in *2013 international conference on biometrics (ICB)*. IEEE, 2013, pp. 1–8.
- [37] Center for Biometrics and Security Research (CBSR), "CASIA iris databases," YEAR-OF-PUBLICATION-OR-LAST-UPDATE, available: <http://www.cbsr.ia.ac.cn/english/IrisDatabase.asp>. [Online]. Available: <http://www.cbsr.ia.ac.cn/english/IrisDatabase.asp>
- [38] R. Shankar, *Principles of quantum mechanics*. Springer Science & Business Media, 2012.
- [39] A. Aspect, "Bell's inequality test: more ideal than ever," *Nature*, vol. 398, no. 6724, pp. 189–190, 1999.
- [40] A. Mair, A. Vaziri, G. Weihs, and A. Zeilinger, "Entanglement of the orbital angular momentum states of photons," *Nature*, vol. 412, no. 6844, pp. 313–316, 2001.

- [41] A. Aspect, P. Grangier, and G. Roger, "Experimental realization of einstein-podolsky-rosen-bohm gedankenexperiment: A new violation of bell's inequalities," *Physical review letters*, vol. 49, no. 2, p. 91, 1982.
- [42] J. F. Clauser, "Early history of bell's theorem," in *Coherence and Quantum Optics VIII: Proceedings of the Eighth Rochester Conference on Coherence and Quantum Optics, held at the University of Rochester, June 13–16, 2001*. Springer, 2003, pp. 19–43.
- [43] T. Palmer, "Bell's conspiracy, schrödinger's black cat and global invariant sets," *Philosophical Transactions of the Royal Society A: Mathematical, Physical and Engineering Sciences*, vol. 373, no. 2047, p. 20140246, 2015.
- [44] J. R. Hance, S. Hossenfelder, and T. N. Palmer, "Supermeasured: Violating bell-statistical independence without violating physical statistical independence," *Foundations of Physics*, vol. 52, no. 4, p. 81, 2022.
- [45] A. Einstein, B. Podolsky, and N. Rosen, "Can quantum-mechanical description of physical reality be considered complete?" *Physical review*, vol. 47, no. 10, p. 777, 1935.
- [46] U. Vazirani and T. Vidick, "Fully device independent quantum key distribution," *Communications of the ACM*, vol. 62, no. 4, pp. 133–133, 2019.
- [47] M. Curty, F. Xu, W. Cui, C. C. W. Lim, K. Tamaki, and H.-K. Lo, "Finite-key analysis for measurement-device-independent quantum key distribution," *Nature communications*, vol. 5, no. 1, p. 3732, 2014.
- [48] H.-K. Lo, M. Curty, and B. Qi, "Measurement-device-independent quantum key distribution," *Physical review letters*, vol. 108, no. 13, p. 130503, 2012.
- [49] L. Masanes, S. Pironio, and A. Acín, "Secure device-independent quantum key distribution with causally independent measurement devices," *Nature communications*, vol. 2, no. 1, p. 238, 2011.
- [50] C. H. Bennett, G. Brassard, and J.-M. Robert, "Privacy amplification by public discussion," *SIAM journal on Computing*, vol. 17, no. 2, pp. 210–229, 1988.
- [51] S. Abruzzo, H. Kampermann, M. Mertz, and D. Bruß, "Quantum key distribution with finite resources: Secret key rates via rényi entropies," *Physical Review A*, vol. 84, no. 3, p. 032321, 2011.
- [52] R. Renner and S. Wolf, "Simple and tight bounds for information reconciliation and privacy amplification," in *International Conference on the Theory and Application of Cryptology and Information Security*. Springer, 2005, pp. 199–216.
- [53] D. J. MacKay and D. J. Mac Kay, *Information theory, inference and learning algorithms*. Cambridge university press, 2003.
- [54] X.-A. Wang and S. B. Wicker, "An artificial neural net viterbi decoder," *IEEE Transactions on communications*, vol. 44, no. 2, pp. 165–171, 1996.
- [55] W. E. Ryan *et al.*, "An introduction to ldpc codes," *CRC Handbook for Coding and Signal Processing for Recording Systems*, vol. 5, no. 2, pp. 1–23, 2004.
- [56] E. Berlekamp, R. McEliece, and H. Van Tilborg, "On the inherent intractability of certain coding problems (corresp.)," *IEEE Transactions on Information Theory*, vol. 24, no. 3, pp. 384–386, 1978.